GRADUATE AERONAUTICAL LABORATORIES
CALIFORNIA INSTITUTE OF TECHNOLOGY

Experimental investigation of planar strained methane-air and ethylene-air flames

Laurent J.-M. Benezech, Jeffrey M. Bergthorson,
and Paul E. Dimotakis

GALCIT Report GALCITFM2006.002

26 MARCH 2006

Firestone Flight Sciences Laboratory

Guggenheim Aeronautical Laboratory

Karman Laboratory of Fluid Mechanics and Jet Propulsion

Pasadena

Experimental investigation of planar strained methane-air and ethylene-air flames

Thesis by

Laurent J.-M. Benezech[1]

In Partial Fulfillment of the Requirements

for the Degree of

Master from CHALMERS in Turbulence

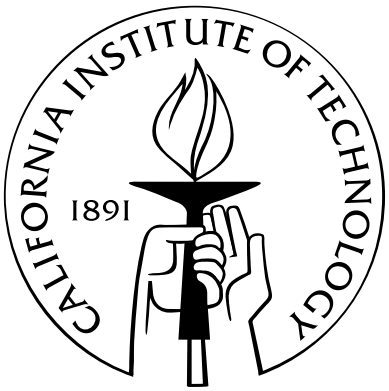

California Institute of Technology

Pasadena, California

2006

(Submitted 26 March 2006)

*Corresponding author.
E-mail address: benezech@tyrvos.caltech.edu

Acknowledgements

This work was carried out at the California Institute of Technology under the direction of Professor Paul Dimotakis. I would like to thank him for providing everything I needed to carry out this work. I am especially grateful for his good advice, and also because he cares about my education and always pushes me to get a better understanding.

I would like to thank Jeff Bergthorson specially, for providing me such a nice starting experimental set-up. During this last year here, I learned a lot and received constant support from him, as an advisor as well as a friend.

I would like to thank Professor David Goodwin for developing the CANTERA software package. I would like to thank Kazuo Sone and George Matheou for their help regarding simulation issues.

I would also like to acknowledge Garrett Katzenstein's helpful technical advice and his mechanical design ideas. The drawings would be nothing without Joe, Brad, and Ali from the Aeronautics machine shop, whose work is remarkable. Dr. Dan Lang's assistance with digital imaging, electronics, data acquisition, and all computer matters is very much appreciated. Christina Mojahedi's efficient help and her numerous advice helped me a lot, the coffee breaks with her are very enjoyable too.

This work was funded by the Air Force Office of Scientific Research, with additional funding through the Caltech Northrop Chair.

From the Swedish university Chalmers, I would like to acknowledge the extremely valuable advice that Dr. Gunnar Johansson gave to me, and I would like to thank Professor William George for making me feel like doing a PhD and for advising me to come here. Both provided a remarkable learning environment, as well as a unique international experience with the International Master's Program in Turbulence. After one year in this program, I gained considerable knowledge in both experimental methods and numerical simulations, but chiefly this program made me want to tackle unresolved problems. Dr. Gunnar Johansson and Professor William George helped me a lot to give a direction to my life that I really enjoy one year later, I would not have had the wonderful opportunity to work at Caltech without them.

Of course, I would like to thank my family who have always been present when emotional support was needed.

Abstract

The extinction of planar strained methane-air flames in the stagnation-point flow is studied. A thermal analysis has been conducted in order to build a new copper stagnation plate which can be heated up to 1000K, and allows investigation of downstream heat loss as extinction driving mechanism.

Since premixed stagnation flames are mostly sensitive to the composition of the mixture, axial velocity and CH radical profiles are simultaneously measured for different equivalence ratios, using respectively Particle Streak Velocimetry (PSV) and Planar Laser Induced Fluorescence (PLIF). These are compared to simulations using CANTERA stagnation flow code with a multicomponent molecular transport model, with the following chemical kinetics mechanisms: GRI-MECH 3.0, the C_3-Davis, San-Diego 200308 and San-Diego 200503 mechanisms. In methane-air flames, simulations accurately predict the velocity and CH profiles from $\Phi = 0.8$ to $\Phi = 1.2$, but the flame speed turns out to be overpredicted at $\Phi = 0.70$ by all mechanisms except the C_3-Davis mechanism (see Bergthorson *et al.* 2005a). The experiment at $\Phi = 1.3$ would need to be reconducted. Also, measured relative concentrations of CH are compared to numerical predictions using each of the four mechanisms cited above. Composition variations impact on ethylene-air flames was also investigated due to a peculiar jump in the overprediction of flame velocities from $\Phi = 1.6$ to $\Phi = 1.8$ (Bergthorson 2005). This peculiar feature was found to be repeatable, but the cause remains unclear.

Methane-air laminar flame speeds S_u^0 were computed using CANTERA freely propagating flame code for the following chemical kinetics mechanisms: GRI-MECH 3.0, the C_3-Davis mechanism, the San Diego 200308, 200503, and 200506 mechanisms, for variable pressures (1,2,5,10,20atm) and equivalence ratios (0.6-1.4). Even for methane, whose chemistry is one of the best understood, the scatter between the different mechanisms is significant. Both composition and pressure were found to affect S_u^0 substantially, although composition variations seem to excite the differences in the predictions among the different mechanisms the most.

Contents

List of Figures

List of Tables

Chapter 1

Introduction

The aim pursued is the assessment of the available experimental database on hydrocarbon flames, in order to validate and further optimize the available chemical kinetics mechanisms. One of the long-term purposes of this project is to capture experimentally the extinction of a flame in the vicinity of walls. Among the advantages of using a stagnation-point flow to study this fast limit phenomenon: the baseline flow is steady, and downstream heat loss can be investigated by changing the wall temperature. The first step towards the extinction capture is mapping its limits as a function of the following key parameters: equivalence ratio, strain, wall temperature. The wall temperature plays a significant role provided downstream heat loss affects the flame extinction. It has been made clear (Yahagi *et al.* 1992) that two distinct extinction modes exist depending on the Lewis number of the deficient reactant: one where flame stretch alone extinguishes the flame, and the other where heat loss is to be taken into account in addition to flame stretch. The Lewis number for a given species is a dimensionless number defined as $Le = \alpha/D$, where α is the heat diffusivity and D is the mass diffusivity of that species. A lean methane/air mixture is characterized by $Le < 1$, the flame is intensified by the Le effect (reactant inflow larger than heat outflow), and the flame can be located close to the stagnation plate, thus the heat loss can affect flame extinction. It is worth noting that low Le (less than 1) flames are associated with relatively low edge-flame velocities (see Nayagam & Williams 2002), which might later help capture the propagation of the flame hole.

Simulations using the Cantera reacting flow software package (Goodwin 2003) were conducted for a lean stagnation methane flame ($\Phi = 0.7$ and $\Phi = 1$) in order to confirm that the wall temperature effect on extinction is significant enough to make a meaningful experiment possible. To be able to use high wall temperatures, a new copper plate has been added to the current experimental set-up, that can be heated up to 1000K. To assist in the design of this plate, a thermal analysis was conducted.

An analysis of the influence of strain rate, nozzle-to-plate separation distance, and dilution shows that these parameters do not alter significantly the flame behavior, compared to changes in the mixture composition (see Bergthorson 2005, Section 5). Therefore, methane-air and ethylene-air flames are studied at different equivalence ratios. Methane was chosen since it is the simplest

possible hydrocarbon fuel molecule; it is also relevant because natural gas typically consists of 90% of methane. Ethane would be the next logical step but performance of the various mechanisms was found to be satisfactory (except for the systematic overprediction of flame velocities with the San-Diego 200308 mechanism) (see Bergthorson & Dimotakis 2006; Bergthorson 2005, Section 5.3). However the double C=C bond present in ethylene is more challenging kinetically. Ethylene is also a good candidate for SCRAMJET propulsion even though its combustion is characterized by modeling uncertainties (Egolfopoulos & Dimotakis 2000). Moreover, a peculiar sudden degradation of the performance of different mechanisms was noticed from $\Phi = 1.6$ to $\Phi = 1.8$ by Bergthorson (2005, Section 5.4.2) that we wish to investigate. That is why ethylene-air flames are also studied here.

Apart from the fuel type and composition, pressure is the key remaining dimension. To assess its effect on flame propagation and the relative performances of the different mechanisms as pressure increases above 1 atm up to moderately high pressures (20 atm), methane-air laminar flame speeds were calculated.

Chapter 2

Chemical kinetics mechanisms

Five chemical kinetics mechanisms were used in this study.

- GRI-Mech 3.0 (Smith *et al.*) is a combustion mechanism developed to model natural gas combustion, including NO formation and reburn chemistry. It contains 53 species and 325 reactions.
- The C_3 mechanism of Davis *et al.* (C_3-Davis, 1999) is developed to describe the combustion of C_1–C_3 hydrocarbons and relies on 71 species and 469 reactions.
- The "San Diego" mechanism (see Bibliography: San Diego mechanism) is developed to model the combustion of C_1–C_3 hydrocarbons. In this approach, the numbers of species and reactions are kept to the minimum needed to describe the systems and phenomena addressed, thereby minimizing as much as possible the uncertainties in the rate parameters employed. 3 versions are used in this study: SD20030830 (39 species, 173 reactions), SD20050310 (39 species, 175 reactions), and SD20050615 (40 species, 175 reactions).

Chapter 3

Experimental method

Planar, strained, premixed, methane-air flames stabilized in a jet-wall stagnation flow are investigated. The apparatus was designed and set up by Bergthorson (2005) and consists of:

- a gas delivery system for metering, measuring, and mixing the individual gas streams;
- a nozzle assembly consisting of a plenum, or turbulence-management section, and a high-contraction-ratio nozzle;
- a water-cooled copper stagnation-plate;
- a built-in-house particle seeder;
- lasers, optics, and detectors for the CH fluorescence and velocimetry diagnostics;
- as well as a system for acquiring pressure, mass-flow, and plate-temperature data.

Simultaneous Particle Streak Velocimetry (PSV) and CH Planar Laser Induced Fluorescence (PLIF) are used respectively to measure axial velocity profiles and relative concentration profiles of the CH radical (Bergthorson *et al.* 2005a). An advantage of PSV is the reduction of particle loading by an order of magnitude or more when compared with LDV or PIV. This is important in flame environments, as the heat capacity (Ancimer *et al.* 1999) and surface-catalytic properties of particles can potentially alter flame/combustion behavior. As for the PLIF, CH is an intermediate species confined to the reaction zone contrary to OH, which has a broad profile (still present in the post-flame region). Hence CH is more suited than OH to provide a sensitive test of strained flame models (Crosley 1989). The measured axial velocity profile and concurrent measurements of mixture composition, static-pressure drop, and stagnation-plate temperature provide accurate boundary conditions for numerical simulations.

Chapter 4

Extinction simulations

Simulations were performed at two equivalence ratios, $\Phi = 0.7$ and $\Phi = 1$, using one-dimensional predictions from the CANTERA software package developed by Goodwin (2003). The chemical kinetics mechanism used was GRI-MECH 3.0 (Smith *et al.*). The mixture-averaged molecular transport model was applied since it is much faster than the multi-component transport model (Kee *et al.* 2003) and was found to be accurate enough for the present purpose. The nozzle-to-plate separation distance was set to 1cm. Bergthorson (2005, Section 5.2.1) showed that this does not affect the generality of the results, since the flowfield of reacting impinging jets is independent of the nozzle-to-plate separation distance, with the nozzle-exit velocity determining the flame position and resulting velocity field. Given the equivalence ratio, the extinction strain rates corresponding, respectively, to wall temperatures of 300K and 1000K were determined by varying the reactants inflow velocity. A hypothetical plug-flow (u derived from the value of $\dot{m}$ given, and $u' = 0$) was set at the domain inlet (located at $l = 1$cm from the stagnation wall, which would result in $l/d = 1$, where d is the experimental nozzle diameter). However when using the one-dimensional streamfunction formulation for constant-density stagnation flows, plug-flow boundary conditions capture the flow only for $l/d = 0.8$ (Bergthorson *et al.* 2005b). This is due to the fact that the outer solution to the one-dimensional stagnation flow equations is a parabola and cannot capture the free-jet behavior (zero gradient region of flow) that is exhibited for $x/d > 1.0$, where x is the distance from the wall. The model is able to capture the flow for $0 < x/d < 0.8$, when a non zero $u'(l)$ is specified. Nevertheless, using plug-flow boundary condition will not alter the extent of extinction strain-rates ranges that we want to determine with this study. The march towards extinction was achieved by increasing the reactant-mixture inlet mass-flux $\dot{m}$. A multicomponent no-flux boundary condition for the species was used at the wall.

Extinction strain rate is determined by calculating the strain rate of the flame closest to extinction in the march. The strain rate, $\sigma = \mathrm{d}u/\mathrm{d}x$, is defined here as the gradient of the velocity profile upstream of the velocity minimum.

Although our approach cannot capture the turning-point behavior (Nishioka *et al.* 1996), Fig. 4.1

shows how close the turning point, and hence extinction, can be approached as the reactant-mixture mass flux is increased. Another method would specify, for example, the [H] peak location and solve for the strain rate instead of setting it as a boundary-condition. This would allow the extinction strain rate to be determined with a higher accuracy as the strain rate value corresponding to the turning point.

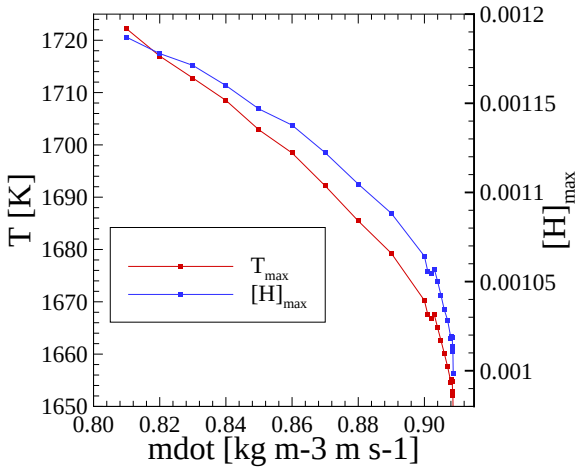

Figure 4.1: Upper-branch S-curve behavior for the $\Phi = 0.70$ methane-air flame

Extinction strain rates at a wall temperature of 300K and 1000K define a range in which the flame can be quenched by varying the wall temperature only; while decreasing the wall temperature, heat loss from the flame to the wall increases and extinction eventually occurs. Extinction strain-rate values were found to be $\sigma(\Phi = 0.7, T_{\text{wall}} = 300\text{K}) = 140$ (1/s), $\sigma(\Phi = 0.7, T_{\text{wall}} = 1000\text{K}) = 175$ (1/s), $\sigma(\Phi = 1, T_{\text{wall}} = 300\text{K}) = 507$ (1/s), and $\sigma(\Phi = 1, T_{\text{wall}} = 1000\text{K}) = 579$ (1/s). Hence the ranges of extinction via T_{wall} in terms of strain rate are

- at $\Phi = 0.7$: [140,175] (1/s)
- at $\Phi = 1$: [507,579] (1/s)

Those results were compared to data from Bergthorson ($T_{\text{wall}} = 350\text{K}$ to 400K), and Egolfopoulos *et al.* (1997) ($T_{\text{wall}} = 573\text{K}$ and 1000K). At $\Phi = 0.7$, the lower limit seems too low when compared to Bergthorson's data (30% relative difference), but compares better (12%) to Egolfopoulos *et al.*'s data at $T_{\text{wall}} = 573\text{K}$; the upper limit seems too high but not far compared to Egolfopoulos *et al.*'s data at $T_{\text{wall}} = 1000\text{K}$ (17%). At $\Phi = 1$, the lower limit is higher than that in Bergthorson's data (21%); the upper limit seems too high but not far compared to that of Egolfopoulos *et al.*'s data at $T_{\text{wall}} = 1000\text{K}$ (19%). To sum up, considering the scattering of the values of the extinction strain-rates at a given Φ in the previous literature, the results obtained thanks to Cantera are accurate enough for our estimates.

While theory predicts a wall-temperature effect on the extinction of lean methane flames, this effect remains weak compared to the impact of the two other parameters, equivalence ratio, and strain rate, hence the importance of setting the strain rate close enough to the extinction strain rate before varying the temperature. The relative extent of the range defined earlier will indicate whether a strain rate sufficiently close to extinction can actually be set experimentally so that the wall-temperature drop will trigger extinction. In our experimental set-up, strain rate can be modified by changing the nozzle-exit velocity of the reactants mixture, without altering mixture composition. This velocity is monitored by a 1 Torr full-scale differential-pressure transducer (BOC Edwards W57401100 and W57011419) that measures the pressure difference between the jet-plenum interior and a point just outside the jet-core flow region (velocity and pressure difference are related by the Bernoulli relation). The relative accuracy of our experimental pressure difference is around 6%. On the other hand, the ranges of extinction via T_{wall} in terms of pressure difference are

- at $\Phi = 0.7$: [0.31-0.48] (Pa)
- at $\Phi = 1$: [4.12-5.22] (Pa)

These ranges respectively exhibit 24% and 43% relative changes. Therefore, it appears that we will be able to get close enough in terms of strain rate so that varying only wall temperature should trigger extinction.

Chapter 5

Thermal analysis of the new plate

For the purposes of the analysis that follows, we will assume that both the lateral and top surfaces are perfectly insulated. Thus we only have to consider the bottom surface of the plate for the heat exchange and its mass for its thermal inertia. The plate is a single copper piece with a ring at the top (inner and outer diameters: $d_\mathrm{i} = 2.5$ in and $d_\mathrm{o} = 3$ in, height: $h_\mathrm{i} = 1.2$ in), and with a cylinder at the bottom (diameter: d_o, height: $h_\mathrm{o} - h_\mathrm{i} = 1.5 - 1.2 = 0.3$ in). In the following thermal analysis, the system considered is the copper plate, heated by the hot (post-flame) impinging jet, and cooled by both radiative and convective loss.

5.1 Heat coming from the flame

$$P_\mathrm{f} = \dot{m}_\mathrm{mix}\ \Delta_\mathrm{c}H^0_\mathrm{mix}\ , \tag{5.1}$$

where

$$\dot{m}_\mathrm{mix} = (\rho_\mathrm{mix}\ U\ S)_\mathrm{nozzle-exit} = 128\ g\ s^{-1}\ , \tag{5.2}$$

$$\Delta_\mathrm{c}H^0_\mathrm{mix} = \Delta_\mathrm{c}H^0\ \frac{Y_{\mathrm{CH_4}}}{W_\mathrm{mix}}\ , \tag{5.3}$$

with $\Delta_\mathrm{c}H^0 = 890.8$ kJ $\mathrm{mol}^{-1}_{\mathrm{CH_4}}$, $Y_{\mathrm{CH_4}} = \frac{1}{10.46}$, $W_\mathrm{mix} = 28$ g mol^{-1}.
Therefore $P_\mathrm{f} = 0.39$ kW

5.2 Convective loss

The jet impinging on the plate entrains some air at ambient temperature. Hence cold air is convected along the bottom surface of the plate, which generates heat loss by convection.

$$P_\mathrm{c} = \dot{m}_\mathrm{entr}\ C_\mathrm{p}\ \Delta T\ , \tag{5.4}$$

where we will assume that

$$\dot{m}_{\rm entr} \sim 5\ \dot{m}_{\rm mix}\ , \tag{5.5}$$

$$C_{\rm p} = C_{\rm p,air}(T_{\rm amb}) \quad \text{in the worst case}\ , \tag{5.6}$$

$$\Delta T = T_{\rm exit} - T_{\rm amb}\ , \tag{5.7}$$

To get an estimate of $T_{\rm exit}$, the characteristic time of heat conduction of air at 1000K (very close to the plate) across the convected air layer is compared to the characteristic time of heat convection from the center to the edge of the plate.

$$\tau_{\rm cv} = \frac{d_{\rm o}/2}{U_{\rm entr}}\ , \tag{5.8}$$

with $U_{\rm entr} \sim 0.7$ m s^{-1}. Hence $\tau_{\rm cv} = 0.054$ s

$$\tau_{\rm cond} = \frac{L^2}{D_{\rm T}}\ , \tag{5.9}$$

with

$$L = \frac{\dot{m}_{\rm entr}}{\rho\ U_{\rm exit}\ \pi\ d_{\rm o}} \quad \text{by mass} - \text{flux conservation}\ , \tag{5.10}$$

The density, ρ, is picked at 750K : 0.46 kg m^{-3} , $L = 4$ mm , $D_{\rm T}(1000{\rm K}) = 1.7\ 10^{-4}$ m^2 s^{-1} , and

$$U_{\rm exit} \sim 20\%\ U_{\rm nozzle-exit} = 0.3\ {\rm m\ s^{-1}}\ , \tag{5.11}$$

Hence $\tau_{\rm cond} = 0.087$ s

Thus $\tau_{\rm cond}$ and $\tau_{\rm cv}$ are of the same order of magnitude, which means that the heat coming from the 1000K plate has time to be conducted through the cold (300K) air-layer convected along the plate. Since heat convection is more effective than conduction, $T_{\rm exit}$ can be estimated as being around 550K. Therefore $P_{\rm c} = 0.16$ kW

5.3 Radiative loss

As pointed out at the beginning of this analysis, only the bottom-surface is asumed to radiate heat from the plate.

$$P_{\rm r} = \epsilon\ \sigma\ (T_{\rm wall}^4 - T_{\rm amb}^4)\ S\ , \tag{5.12}$$

where $\epsilon = 0.85$ in the worst case, $\sigma = 5.6705\ 10^{-8}$ W/(m^{2}K^4) , $T_{\rm amb} = 300$K , and

$$S = \pi\ \frac{d_{\rm o}^2}{4} \tag{5.13}$$

T_{wall} (K)	P_{r} (kW)
300	0
400	0.004
500	0.012
600	0.027
700	0.051
800	0.088
900	0.142
1000	0.218

Table 5.1: Radiative heat-loss for different wall-temperatures.

Therefore, in the worst case ($T_{\text{wall}} = 1000\text{K}$), $P_{\text{r}} = 0.22$ kW

5.4 Plate thermal inertia

Given the net power applied to the plate, the time required for a given change in temperature of the plate can be deduced.

$$\tau = \frac{m_{\text{Cu}}\ C_{\text{p,Cu}}\ \Delta T}{P_{\text{net}}}\ , \tag{5.14}$$

where

$$m_{\text{Cu}} = \rho_{\text{Cu}}[\pi\ \frac{d_{\text{o}}^2}{4}\ (h_{\text{o}} - h_{\text{i}}) + \pi\ \frac{d_{\text{o}}^2 - d_{\text{i}}^2}{4}\ h_{\text{i}}]\ , \tag{5.15}$$

with $\rho_{\text{Cu}} = 8920$ kg m^{-3}

τ (min)	ΔT (K)	100	700
P_{net} (kW)			
0.01		47.1	329.5
0.1		4.7	32.9
1		0.5	3.3

Table 5.2: Heating time of the plate given the net power applied to it and the change in temperature.

From the estimates derived above, the net power applied to the plate in the worst case can be deduced to be:

$$P_{\text{net}} = P_{\text{f}} - P_{\text{c}} - P_{\text{r}} \tag{5.16}$$

Hence $P_{\text{net}} = 0.01$ kW.

Considering the uncertainty on both the radiative loss (which can only be less, with an actual emissivity smaller than the worst case of 0.85) and the convective loss (which could be either smaller or bigger), an additional source of heat should be considered. An interesting solution would be to use a combustible gas mixture in the co-flow, whose current purpose is solely to stabilize the flame by flowing helium (helium density matches that of the combustion products).

Chapter 6

Methane-air flame chemistry effects

6.1 Velocity and normalized CH profiles

Both PSV and CH PLIF diagnostics were applied to methane-air flames as a function of equivalence ratio Φ. The results were compared to Cantera simulations. Unless otherwise indicated, the flames are simulated with the GRI-Mech 3.0 thermo-chemistry/transport model (Smith *et al.*), and a multi-component transport formulation (Kee *et al.* 2003). In earlier studies (Bergthorson 2005, Section 5.2.1), results were found to be insensitive to the nozzle-to-plate separation distance. Therefore, the separation distances were scaled by the nozzle diameter $L/d = 0.8$ for the whole series of experiments.

For the CH PLIF profiles presented here, the laser power was 15mJ/pulse, which results in a saturated laser spectral intensity of $I_\nu = E_\mathrm{p}/(\tau_\mathrm{p} A_\mathrm{b} SW) \approx 10^8$ $(\mathrm{W/cm^2})/\mathrm{cm^{-1}}$, where E_p is the pulse energy, τ_p the pulse length, A_b the laser beam cross-sectional area, and SW the laser spectral width. Although the laser sheet was made as uniform as possible, some non-uniformities may still be present. Flames were therefore kept at the same distance from the wall to ensure that CH radicals were excited at the same laser power, which allows us to compare relative CH peak intensities.

PSV measurements are performed using $1\,\mu$m alumina particles ($\rho_\mathrm{p} \cong 3830\,\mathrm{kg/m^3}$), and the chopping frequencies are $\nu_\mathrm{c} = 1.8$kHz for the slower $\Phi = 0.70, 1.29$ flames, and $\nu_\mathrm{c} = 2.4$kHz for the faster $\Phi = 0.80, 0.90, 1.01, 1.10, 1.20$ flames, respectively. To perform detailed comparisons between simulations and experiment, systematic differences between simulated and measured velocity profiles must be accounted for. In particle-tracking velocimetry techniques, the particle may not track the fluid velocity due to the combined effects of thermophoresis and particle inertia (Bergthorson & Dimotakis 2005). In addition, the finite time interval in particle tracking techniques can act as a spatial low-pass filter. Therefore, the motion of a particle through the simulated flowfield should be modeled using a Lagrangian technique. The PSV analysis methodology is applied to the resulting

particle position-time record, correcting for the finite particle-track interval. These corrections have been applied to all simulated profiles in this section.

Figures 6.1, 6.3, 6.5, 6.7, 6.9, 6.11, and 6.13 plot the PSV,Cantera and Bernoulli velocities, as well as the CH PLIF and Cantera profiles, from $\Phi = 0.70$ to $\Phi = 1.29$. The flame at $\Phi = 1.29$ was studied closer to the nozzle because heat loss to the wall prevented the flame from stabilizing further away. Figures 6.15, 6.17, and 6.19 compare the performances of the four mechanisms used to simulate a lean, stoichiometric, and rich flame. Figures extracted from Bergthorson (2005) are displayed side by side for comparison.

As in Bergthorson *et al.* (2005a), predictions of velocity and CH profiles agree with experiment from $\Phi = 0.80$ to $\Phi = 1.2$, but the flame speed turns out to be overpredicted at $\Phi = 0.70$ by all mechanisms except the C_3-Davis mechanism. At $\Phi = 1.3$, all predictions overpredict flame speeds, whereas predictions match experimental data in Bergthorson *et al.* (2005a). The experiment at that equivalence ratio will need to be redone. Except for the latter flame, the direct comparison between predicted and experimental profiles gave results comparable to those in Bergthorson *et al.* (2005a), although that study and the present study are totally independent, which validates the method used here.

Even for methane, whose chemistry is one of the best understood, the scatter between the different mechanisms is pretty significant. This scatter is expected to be larger for flames with a larger heat-release such as ethylene flames.

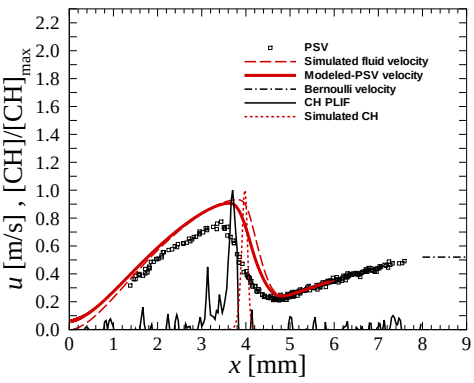

Figure 6.1: $\Phi = 0.70$, CH_4-air flame profiles.

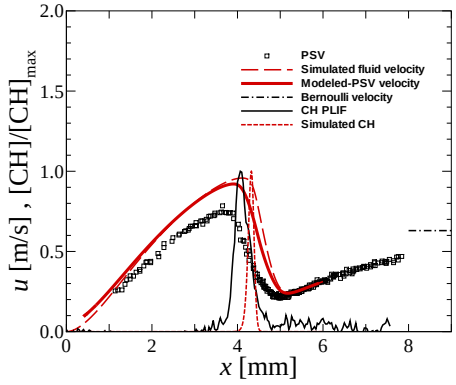

Figure 6.2: $\Phi = 0.7$, CH_4-air flame profiles. Extracted from Bergthorson (2005) Section 5.2.4.

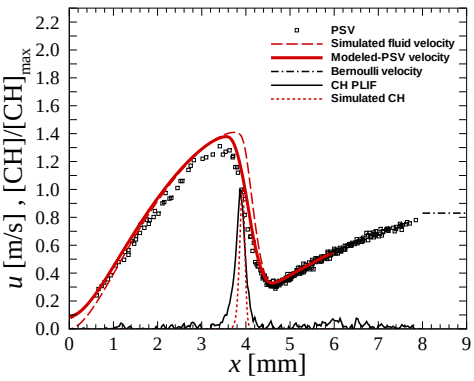

Figure 6.3: $\Phi = 0.80$, CH_4-air flame profiles.

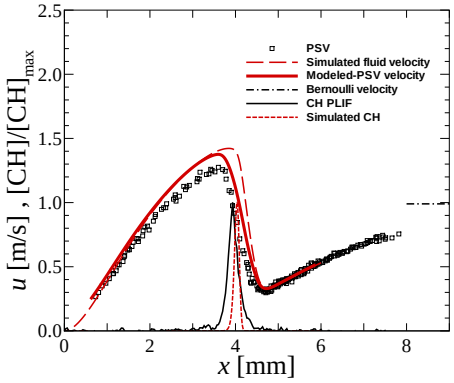

Figure 6.4: $\Phi = 0.8$, CH_4-air flame profiles. Extracted from Bergthorson (2005) Appendix G.

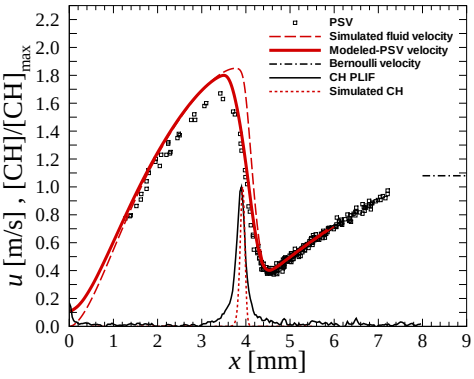

Figure 6.5: $\Phi = 0.90$, CH_4-air flame profiles.

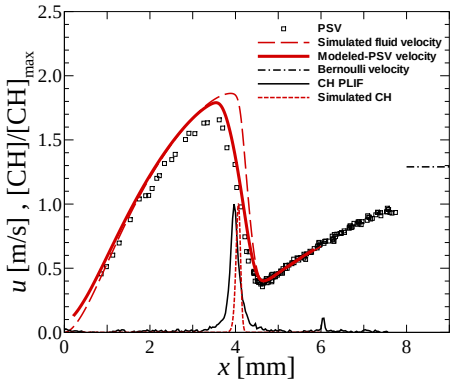

Figure 6.6: $\Phi = 0.9$, CH_4-air flame profiles. Extracted from Bergthorson (2005) Appendix G.

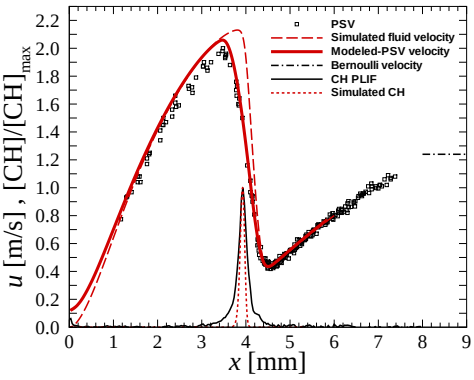

Figure 6.7: $\Phi = 1.01$, CH_4-air flame profiles.

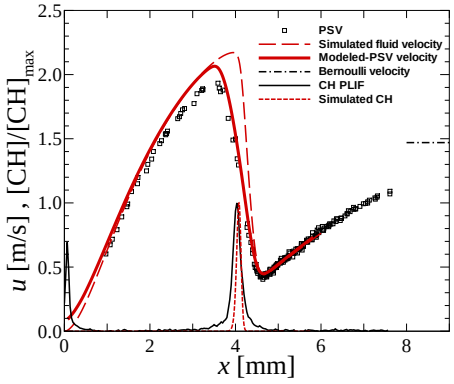

Figure 6.8: $\Phi = 1.0$, CH_4-air flame profiles. Extracted from Bergthorson (2005) Section 5.2.4.

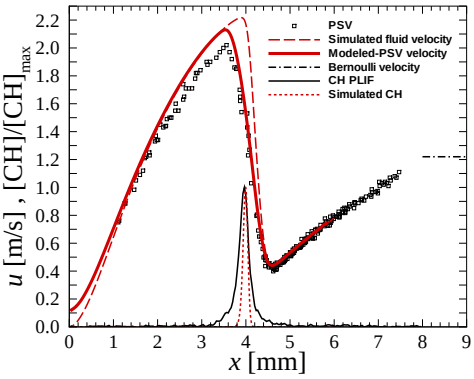

Figure 6.9: $\Phi = 1.10$, CH_4-air flame profiles.

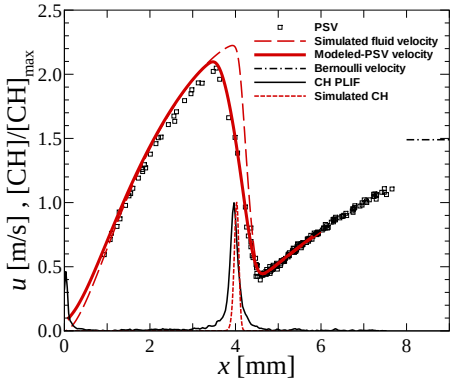

Figure 6.10: $\Phi = 1.1$, CH_4-air flame profiles. Extracted from Bergthorson (2005) Appendix G.

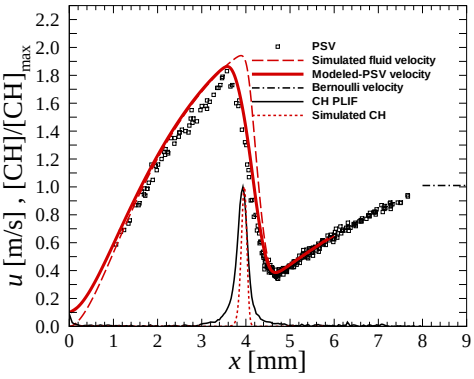

Figure 6.11: $\Phi = 1.20$, CH_4-air flame profiles.

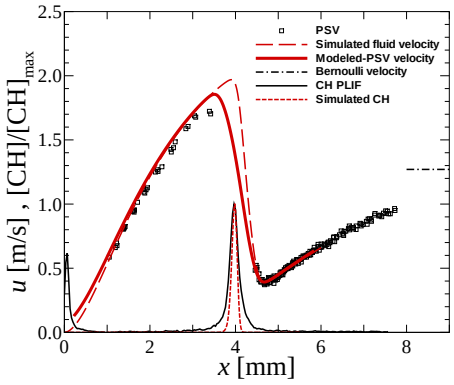

Figure 6.12: $\Phi = 1.2$, CH_4-air flame profiles. Extracted from Bergthorson (2005) Appendix G.

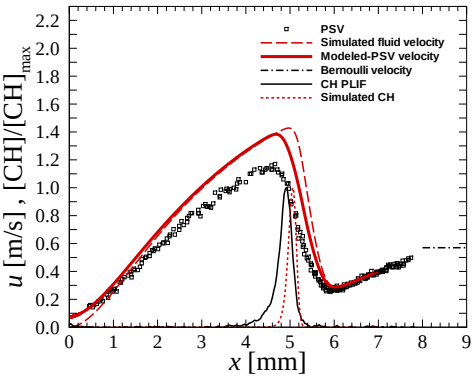

Figure 6.13: $\Phi = 1.29$, CH_4-air flame profiles.

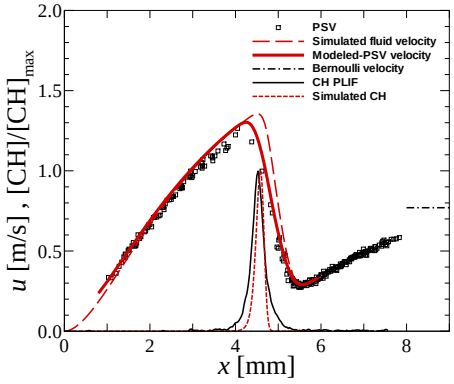

Figure 6.14: $\Phi = 1.3$, CH_4-air flame profiles. Extracted from Bergthorson (2005) Section 5.2.4.

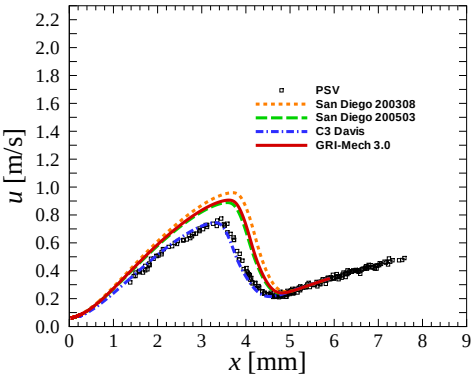

Figure 6.15: Comparison of modeled-PSV profiles to the experimental velocity profile in a $\Phi = 0.70$ CH_4-air flame.

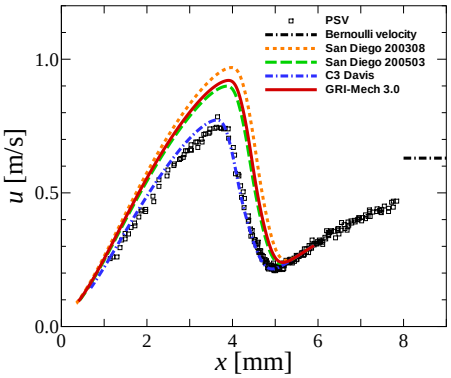

Figure 6.16: Comparison of modeled-PSV profiles to the experimental velocity profile in a $\Phi = 0.7$ CH_4-air flame. Extracted from Bergthorson (2005) Section 5.2.4.

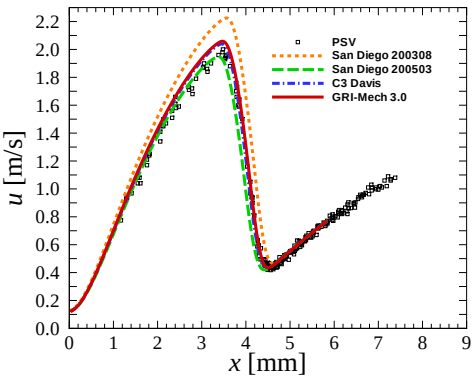

Figure 6.17: Comparison of modeled-PSV profiles to the experimental velocity profile in a $\Phi = 1.01$ CH_4-air flame.

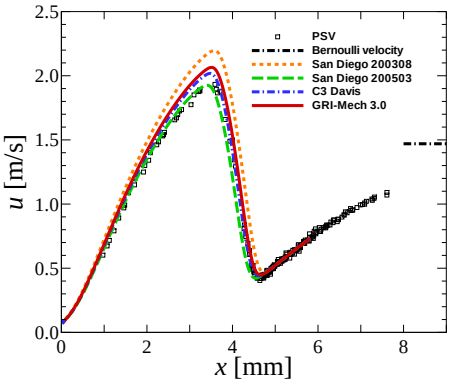

Figure 6.18: Comparison of modeled-PSV profiles to the experimental velocity profile in a $\Phi = 1.0$ CH_4-air flame. Extracted from Bergthorson (2005) Section 5.2.4.

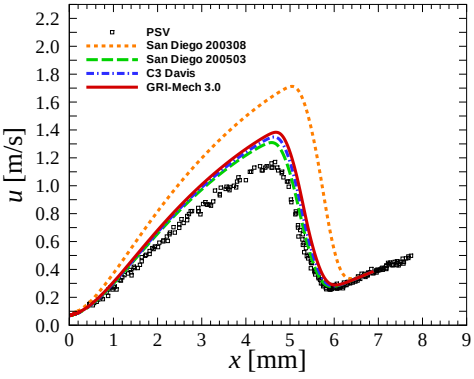

Figure 6.19: Comparison of modeled-PSV profiles to the experimental velocity profile in a $\Phi = 1.29$ CH_4-air flame.

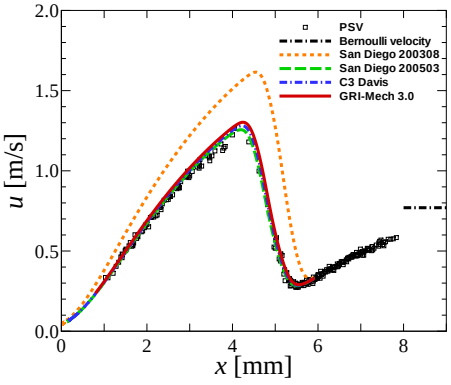

Figure 6.20: Comparison of modeled-PSV profiles to the experimental velocity profile in a $\Phi = 1.3$ CH_4-air flame. Extracted from Bergthorson (2005) Section 5.2.4.

6.2 Relative concentration measurements of CH

Measured CH peak concentrations relative to $\Phi = 1.2$ are compared to numerical predictions using different mechanisms in Fig. 6.21. It is worth noting that off-resonance (also called off-line) images are substracted at each Φ, instead of substracting no-flame images (see Bergthorson 2005, Appendix C). Fig. 6.23 shows that the off-resonance signal weight relative to the raw signal becomes significantly higher at $\Phi = 0.70$ 0.80 1.29 than at $\Phi = 1.20$, therefore the CH concentration would have been overestimated in the leanest and richest flames if the no-flame substraction had been performed.

Sutton & Driscoll (2003) found that the maximum CH signal occurs for $\Phi = 1.25$, and that the relative CH concentrations at $\Phi = 1.15$ and 1.35 are comparable, which is different from the data presented here. In both the present study and that of Sutton & Driscoll (2003), respective simulations using the GRI-Mech 3.0 mechanism tend to agree with the data. What Bergthorson (2005, Section 5.2.5) inferred about his data can be applied to the data presented here as well: the relative CH concentrations (as a function of stoichiometry) are dependent on the experimental configuration, and a direct comparison with data from Sutton & Driscoll may not be valid. In both the present analysis and that of Sutton & Driscoll (2003), numerical predictions show a stronger variation in the relative CH concentration as a function of Φ than the experimental results, and the predicted relative CH concentrations are below that measured using the PLIF technique.

The primary goal of the variable composition methane-air flame experiments was to validate the experimental method by comparison with Bergthorson's direct comparisons between predicted and experimental profiles. But additional care was taken in maintaining the PLIF laser power constant and in recording the off-line signal to provide relative CH peak concentrations data, which are scarce. The two different studies show the same results here, which is impressive, even if the saturated laser spectral intensity was the same in each of them.

Table 6.1 summarizes the features of the flames discussed above.

exp #	Φ	$\%O_2$:(O_2+N_2)	σ [1/s]	$S_{u,ref}$ [m/s]
068	1.29	21.0	133	0.272
069	1.20	21.0	216	0.379
070	1.10	21.0	275	0.432
071	1.01	21.0	271	0.439
072	0.90	21.0	241	0.39
073	0.80	21.0	182	0.316
074	0.70	21.0	102	0.218

Table 6.1: Reference flame speeds at various imposed strain rates for methane experiments.

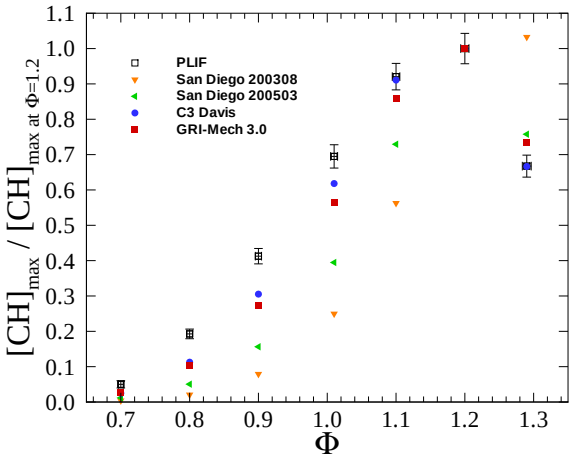

Figure 6.21: Comparison of measured peak concentrations of CH relative to $\Phi = 1.20$ to predicted results using three different chemical mechanisms.

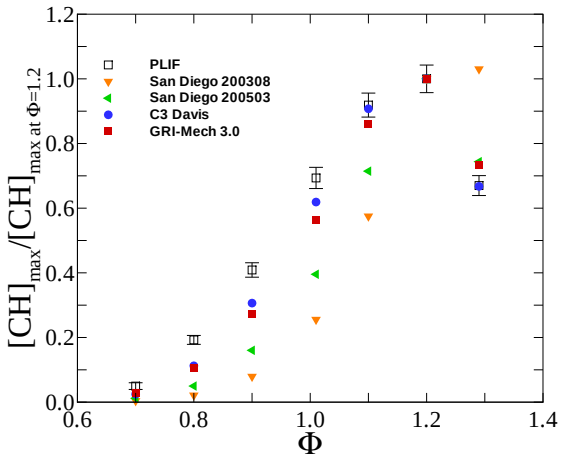

Figure 6.22: Comparison of measured peak concentrations of CH relative to $\Phi = 1.20$ to predicted results using three different chemical mechanisms. Extracted from Bergthorson (2005) Section 5.2.5.

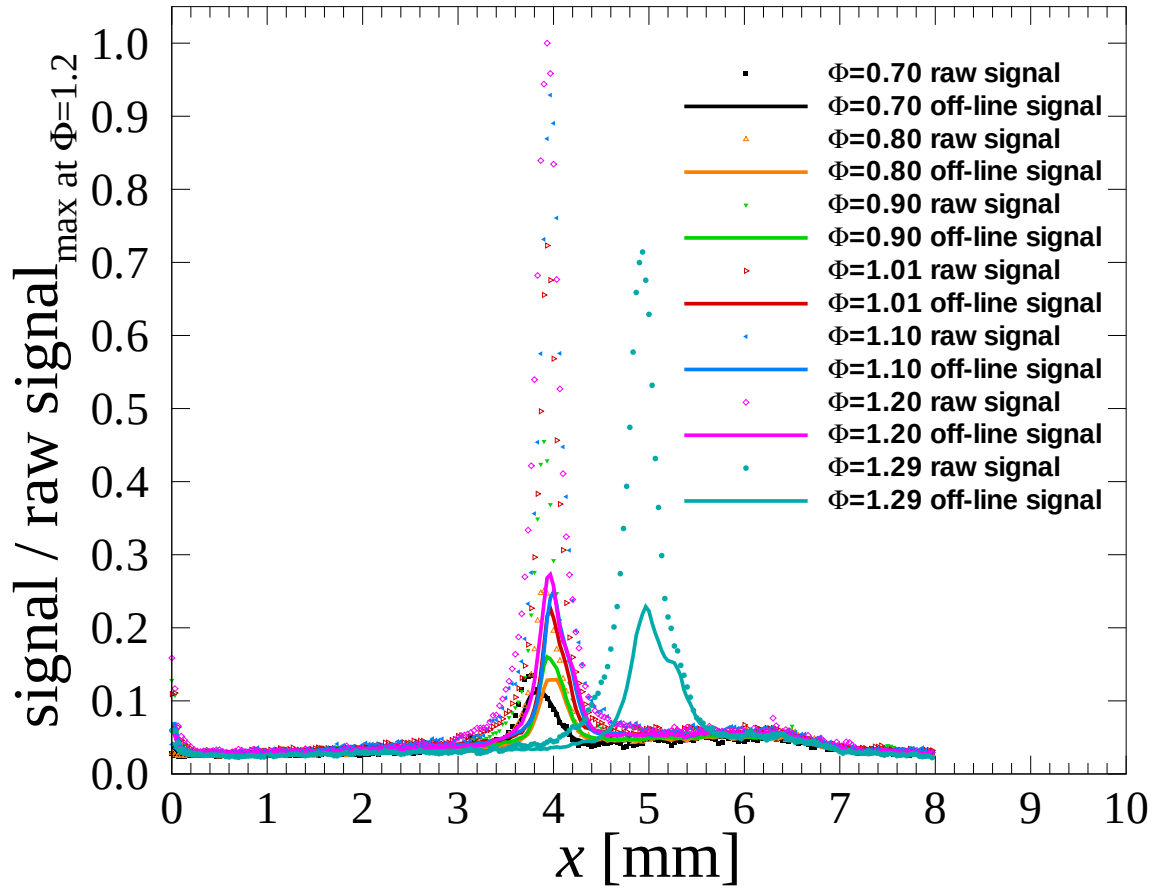

Figure 6.23: Raw signal and Off-line signal for different Φ.

Chapter 7

Ethylene-air flame chemistry effects

Experiments on ethylene-air flames of varying composition have already been conducted (Bergthorson & Dimotakis 2006). However the departure of predicted CH peak locations from the experimental value suddenly jumps when Φ is increased from 1.6 to 1.8. The experiments are therefore repeated here to confirm the previous results.

Due to the higher velocities involved in ethylene combustion, the current velocimetry diagnostic is not able to resolve velocity profiles with a high enough spatial resolution. The stoichiometric and $\Phi = 1.4$ flames are therefore diluted (model performance is independent of flame speed). For the CH PLIF profiles presented here, the laser power was 10mJ/pulse, which results in a saturated laser spectral intensity of $I_\nu = E_\mathrm{p}/(\tau_\mathrm{p} A_\mathrm{b} SW) \approx 10^8$ (W/cm^2)/cm^{-1}. Despite a lower energy per pulse (10mJ versus 15mJ), reducing the cross-sectional height of the beam allowed the same saturated laser spectral intensity as in the methane-air studies. PSV measurements are performed using $1\,\mu$m alumina particles ($\rho_\mathrm{p} \cong 3830\,\mathrm{kg/m^3}$), and the chopping frequencies are $\nu_\mathrm{c} = 2.0$kHz for the slower $\Phi = 0.60, 1.80$ flames, and $\nu_\mathrm{c} = 2.4$kHz for the faster $\Phi = 1.00, 1.40, 1.60$ flames, respectively. All the simulated velocity profiles shown here are corrected for the effects of thermophoresis, particle inertia, and finite chopping frequency.

Figures 7.1, 7.3, 7.5, 7.7, and 7.9 plot the PSV, Cantera and Bernoulli velocities, as well as the CH PLIF and Cantera profiles using the San-Diego 200503 mechanism. This was shown by Bergthorson & Dimotakis (2006) to have the best performance out of the mechanisms used here when simulating ethylene-oxygen-nitrogen flames, at least for the following equivalence ratios: $\Phi = 0.60, 1.00, 1.40, 1.60, 1.80$. The flame at $\Phi = 1.80$ was studied closer to the nozzle because heat loss to the wall prevented it from stabilizing further away. Figures 7.11, 7.13, 7.16, and 7.17 compare the performances of the four mechanisms used to simulate a lean, a stoichiometric, as well as the two richest flames. Figures extracted from Bergthorson (2005) are also displayed side by side for comparison.

The results presented here are very similiar to those in Bergthorson (2005, Section 5.4.2), although the two studies are totally independent. By contrast to the prediction at $\Phi = 1.6$, the richest $\Phi = 1.80$ flame is predicted significantly more upstream, than the measured one with a higher speed, by all three mechanisms. This might be due to the presence of soot whose production and radiative losses are not taken into account in the model, however no glow was observed for the richest $\Phi = 1.80$ flame. The discrepancy might therefore be due to the appearance of higher-order hydrocarbons that are not present in the mechanisms used. The results of this diluted ethylene-air flames study provide a useful reference for the future investigation of pure ethylene-air flames, thanks to the new velocimetry technique discussed in the Future Work section.

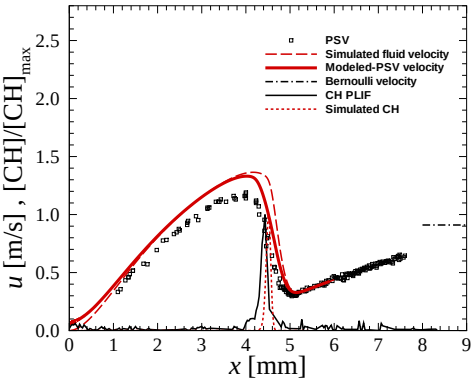

Figure 7.1: $\Phi = 0.60$, 21 %O_2:(O_2+N_2) C_2H_4-air flame profiles.

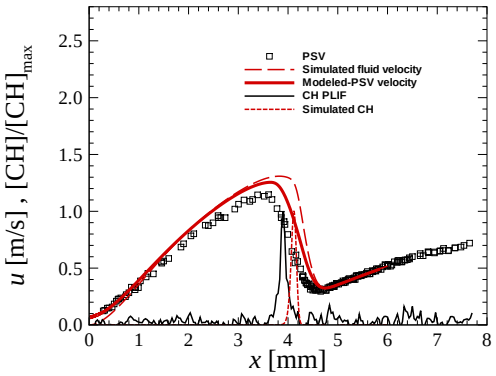

Figure 7.2: $\Phi = 0.6$, 21 %O_2:(O_2+N_2) C_2H_4-air flame profiles. Extracted from Bergthorson (2005) Section 5.4.2.

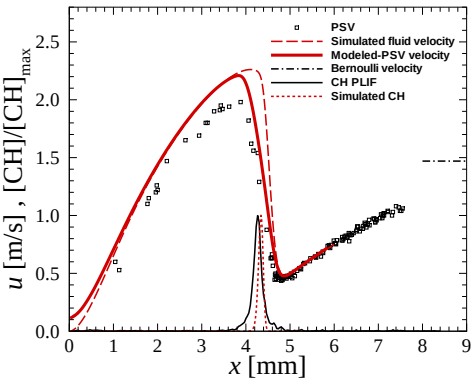

Figure 7.3: $\Phi = 1.00$, 17 %O_2:(O_2+N_2) diluted C_2H_4-air flame profiles.

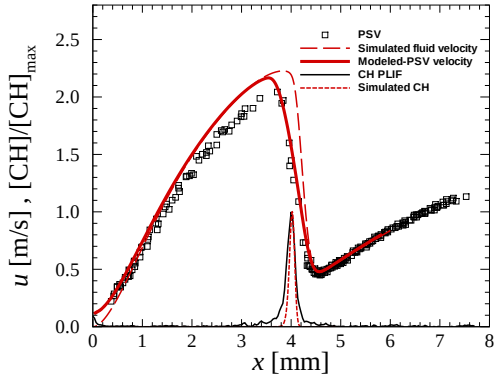

Figure 7.4: $\Phi = 1.0$, 17 %O_2:(O_2+N_2) diluted C_2H_4-air flame profiles. Extracted from Bergthorson (2005) Section 5.4.2.

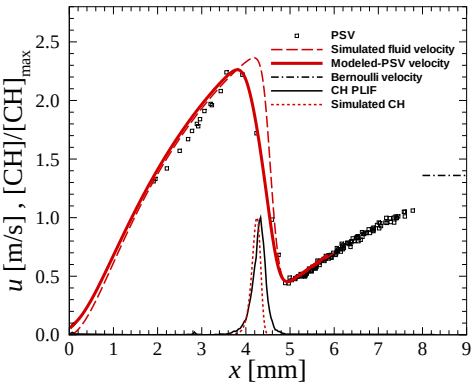

Figure 7.5: $\Phi = 1.40$, 18.0 %O_2:(O_2+N_2) diluted C_2H_4-air flame profiles.

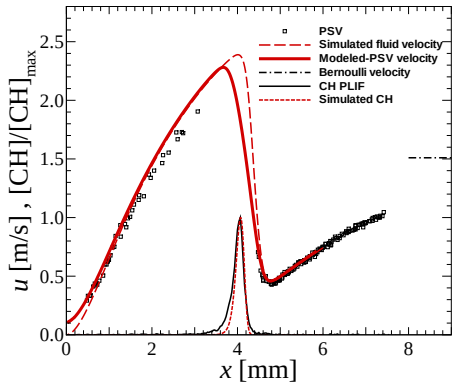

Figure 7.6: $\Phi = 1.4$, 18.0 %O_2:(O_2+N_2) diluted C_2H_4-air flame profiles. Experimental data extracted from Bergthorson (2005) Appendix I, PSV corrections applied to Bergthorson's simulations.

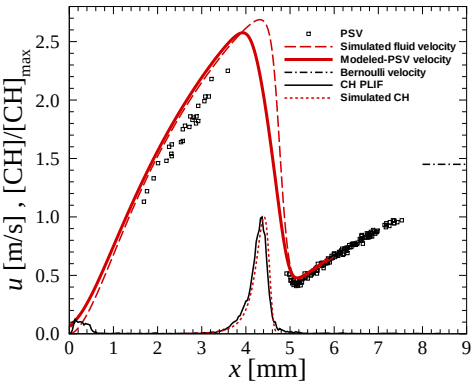

Figure 7.7: $\Phi = 1.60$, 21.0 %O_2:(O_2+N_2) C_2H_4-air flame profiles.

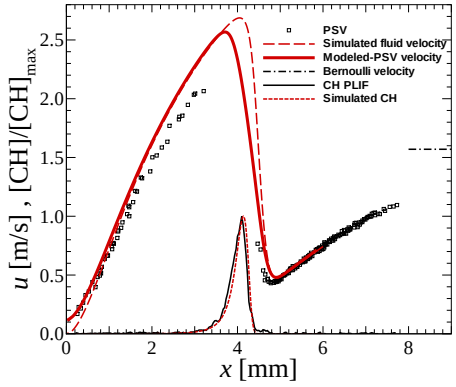

Figure 7.8: $\Phi = 1.6$, 21.0 %O_2:(O_2+N_2) C_2H_4-air flame profiles. Experimental data extracted from Bergthorson (2005) Appendix I, PSV corrections applied to Bergthorson's simulations.

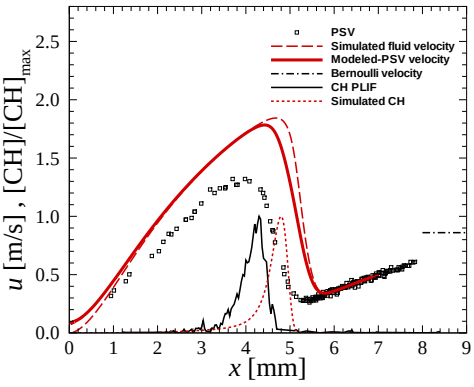

Figure 7.9: $\Phi = 1.80$, 21 %O_2:(O_2+N_2) C_2H_4-air flame profiles.

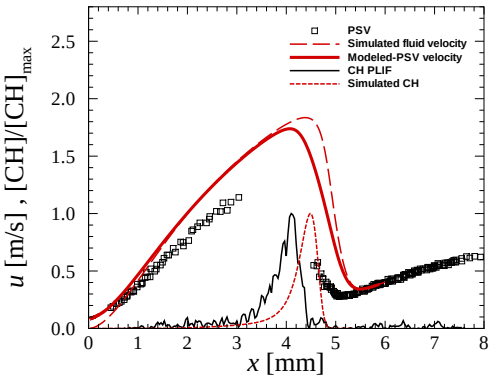

Figure 7.10: $\Phi = 1.8$, 21 %O_2:(O_2+N_2) C_2H_4-air flame profiles. Extracted from Bergthorson (2005) Section 5.4.2.

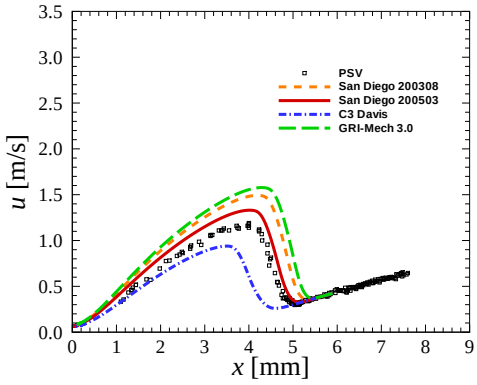

Figure 7.11: Comparison of modeled-PSV profiles to the experimental velocity profile in a $\Phi = 0.60$, 21 %O_2:(O_2+N_2) C_2H_4-air flame.

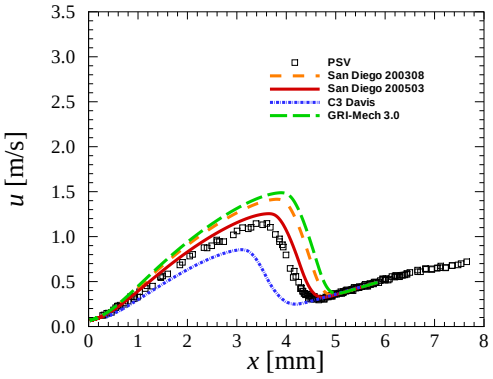

Figure 7.12: Comparison of modeled-PSV profiles to the experimental velocity profile in a $\Phi = 0.6$, 21 %O_2:(O_2+N_2) C_2H_4-air flame. Extracted from Bergthorson (2005) Section 5.4.2.

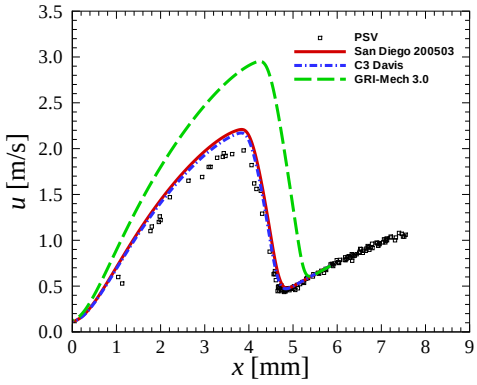

Figure 7.13: Comparison of modeled-PSV profiles to the experimental velocity profile in a $\Phi = 1.00$, 17 %O_2:(O_2+N_2) C_2H_4-air flame.

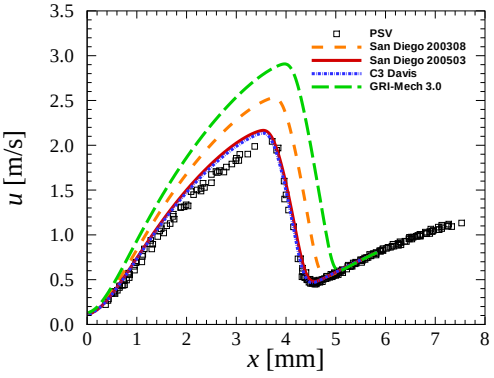

Figure 7.14: Comparison of modeled-PSV profiles to the experimental velocity profile in a $\Phi = 1.0$, 17 %O_2:(O_2+N_2) C_2H_4-air flame. Extracted from Bergthorson (2005) Section 5.4.2.

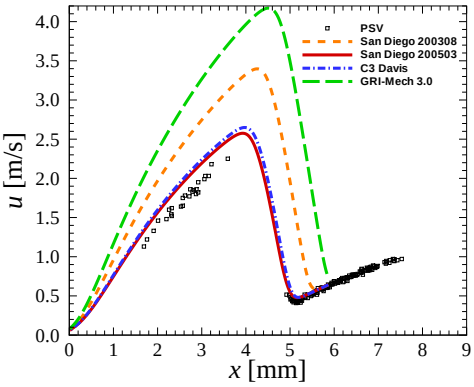

Figure 7.15: Comparison of modeled-PSV profiles to the experimental velocity profile in a $\Phi = 1.60$, 21 %O_2:(O_2+N_2) C_2H_4-air flame.

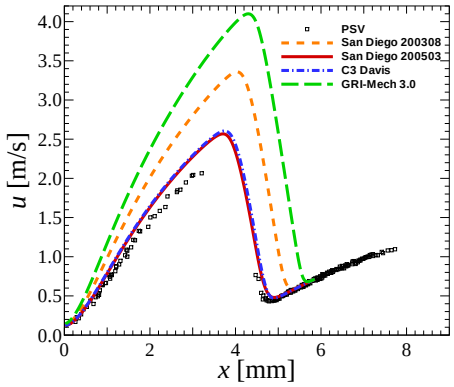

Figure 7.16: Comparison of modeled-PSV profiles to the experimental velocity profile in a $\Phi = 1.6$, 21 %O_2:(O_2+N_2) C_2H_4-air flame. Experimental data extracted from Bergthorson (2005) Appendix I, PSV corrections applied to Bergthorson's simulations.

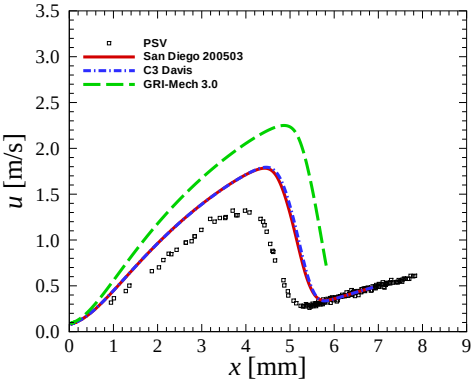

Figure 7.17: Comparison of modeled-PSV profiles to the experimental velocity profile in a $\Phi = 1.80$, 21 %O_2:(O_2+N_2) C_2H_4-air flame.

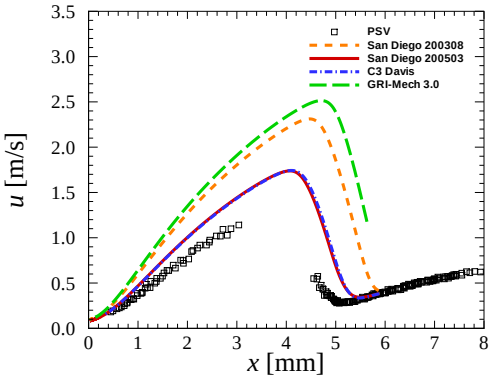

Figure 7.18: Comparison of modeled-PSV profiles to the experimental velocity profile in a $\Phi = 1.8$, 21 %O_2:(O_2+N_2) C_2H_4-air flame. Extracted from Bergthorson (2005) Section 5.4.2.

Table 7.1 summarizes the features of the flames discussed above.

exp #	Φ	$\%O_2 : (O_2 + N_2)$	σ [1/s]	$Suref$ [m/s]
078	1.80	21.0	141	0.278
079	1.60	21.0	278	0.435
080	1.40	18.0	258	0.474
081	1.00	17.0	268	0.45
082	0.60	21.0	152	0.315

Table 7.1: Reference flame speeds at various imposed strain rates for ethylene experiments.

Chapter 8

Laminar flame speeds of methane-air mixtures

Laminar flame speeds S_u^0 are computed for a methane-air flame using the adiabatic, freely propagating flame code available in Cantera release 1.6.0 for five different chemical-kinetics mechanisms (GRI-Mech 3.0, C3-DAVIS, SD20030830, SD20050310, and SD20050615), using both mixture-averaged and multicomponent transport models, and with the number of grid-points close to 1000. The domain length was adjusted to 3 cm, so that gradients nearly vanish at both boundaries. Hence losses of species or energy from the system are negligible.

8.1 Convergence study

The mechanism used in this study is GRI-Mech 3.0, and the transport model used is mixture-averaged. The percent error relative to the solution with the maximum number of grid points, N, is calculated for simulations at varying resolution, i, in the following way: $100 \times (S_{u,i}^0 - S_{u,N}^0)/S_{u,N}^0$.

On Fig. 8.1, the values are seen to asymptote with a difference of less than 0.5 % when the number of grid points exceeds 1000.

Considering the large scatter of the results obtained using different mechanisms, high accuracy of laminar flame speeds is not expected, however 1000 gridpoints are required to compare accurately the different mechanisms.

8.2 Comparison of mixture-averaged and multicomponent transport models

Three main classes of transport coefficients exist (Kee *et al.* 2003): properties for pure species, mixture-averaged transport properties, and multicomponent transport properties. The mixture-averaged transport formulas are less rigorous and computationally much less expensive than the

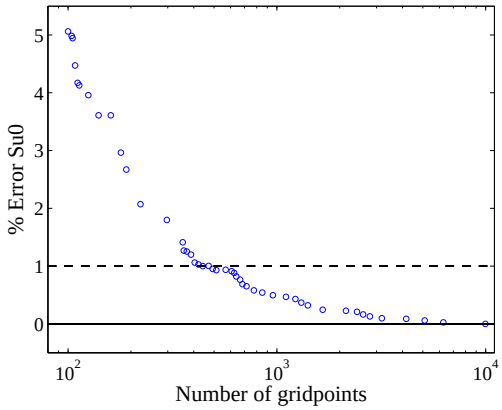

Figure 8.1: Variation of the percent relative error due to resolution, on the laminar flame speed of a $\Phi = 1.0$ methane-air flame.

multicomponent forms. The multicomponent transport properties are based on the formulation of Dixon-Lewis (1968). They are founded on more rigorous theory, but are accompanied by increase in computational cost.

Although multicomponent solutions did not converge for every combination of pressure and equivalence ratio, chiefly in rich conditions and at high pressures, some conclusions can be drawn from Fig. 8.2 and Fig. 8.3 that compare laminar flame speeds predicted by both models over a range of equivalence ratios and pressures.

Fig. 8.2 shows that the relative error between both models seems to be minimum around stoichiometric conditions. Fig. 8.3 suggests that the relative error asymptotes towards a maximum value, as pressure increases. Over the range of equivalence ratios and pressures studied, the percent relative error stays within the range 1%-3.5%, which is a success for the mixture-averaged model. This is due to the oxidizer that is used here, air, which for most species of interest can be considered as existing in trace concentrations compared to the abundant carrier gas N_2, and under such conditions the mixture-averaged coefficients can be quite satisfactory (Kee *et al.* 2003).

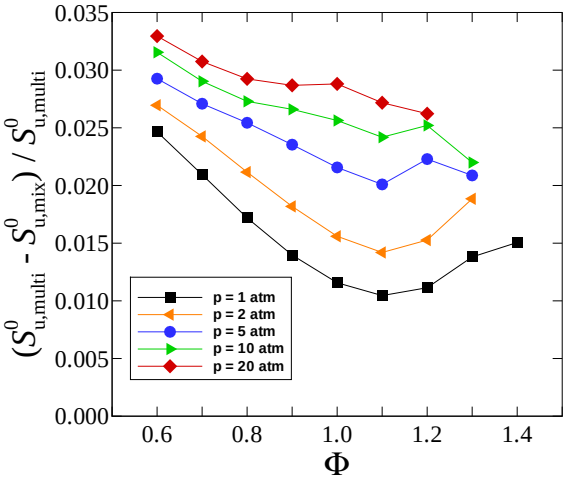

Figure 8.2: Comparison of mixture-averaged and multicomponent laminar flame speeds of a methane-air flame, plotted against equivalence ratio.

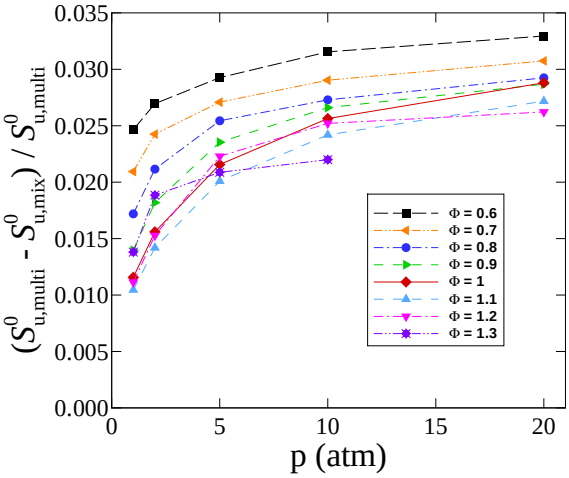

Figure 8.3: Comparison of mixture-averaged and multicomponent laminar flame speeds of a methane-air flame, plotted against pressure.

8.3 Dependence of laminar flame speed on initial temperature

The mechanism used in this study is GRI-Mech 3.0, and the transport model used is multicomponent. Figure 8.4 shows the variation of the laminar flame speed for a stoichiometric methane-air flame with mixture's initial temperature $T_{-\infty}$ over the range 280-700K, and compares the predicted values to the following empirical correlation law (Metghalchi & Keck 1980):

$$S_u^0 = S_{u,ref}^0 \left(\frac{T}{T_{ref}}\right)^{\alpha_T} \left(\frac{P}{P_{ref}}\right)^{\beta_P} \quad \text{(m/s)} \ , \tag{8.1}$$

where (Gu *et al.* 2000) $S_{u,ref}^0 = 0.360$ m/s is the laminar flame speed at a reference temperature $T_{ref} = 300$ K and at a reference pressure $P_{ref} = 0.1$ MPa. The parameters α_T and β_P, which depend upon Φ, when optimized over the full experimental range of 300-400K, and 0.1-1.0 MPa, give: $\alpha_T = 1.612$ and $\beta_P = -0.374$, for $\Phi = 1$. Here, the standard deviation between our predictions and Eq. 8.1 is 0.005.

The linear regime for small changes in $T_{-\infty}$, and the non-linear regime for large variations of $T_{-\infty}$ are explained in Egolfopoulos' lecture notes (2001). In the first case, the kinetic effect is unimportant as $T_{+\infty}$ is minimally affected, the density effect is the dominant one and the flame speed increases nearly linearly with $T_{-\infty}$. In the second case, kinetics starts to be affected through $T_{+\infty}$.

Fig. 8.5 shows how laminar flame speed is sensitive to initial temperature close to ambient temperature (typically 294K in the laboratory). A change in initial temperature from 292K to 296K (a 1.4% relative difference) results in a relative change in S_u^0 of 2.1%. Since such a change in ambient temperature is possible in the laboratory, a measurement of the initial temperature of the combustible mixture will be added to the current suite of diagnostics, so that inlet temperature can be set more acccurately in the 1D stagnation flame simulations.

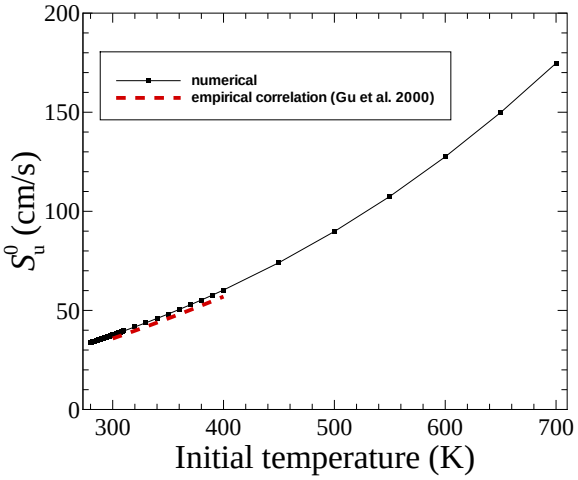

Figure 8.4: Variation of laminar flame speed with initial temperature, for a stoichiometric methane-air flame at atmospheric pressure.

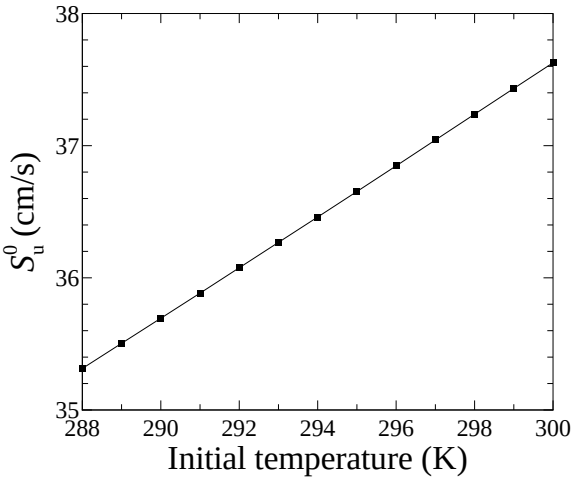

Figure 8.5: Variation of laminar flame speed with initial temperature close to ambient temperature, for a stoichiometric methane-air flame at atmospheric pressure.

8.4 Dependence of flame thickness on pressure

The flame thickness is calculated for a stoichiometric methane-air flame simulated with GRI-Mech 3.0using two different methods. The first one is the tangent method, which determines the distance, $\delta_{\text{max slope}}$, between the intersection of the straight line tangent to the temperature profile at the point of maximum gradient with the temperatures of the unburned and burned states. The second one defines the flame thickness, $\delta_{\text{[CH] FWHM}}$, as the full width at half maximum (FWHM) of the predicted [CH] profile. Fig. 8.6 shows that $\delta_{\text{max slope}}$ is approximately five times larger than $\delta_{\text{[CH] FWHM}}$ over the range of pressures studied. Fig. 8.7 shows that flame thickness drops significantly as pressure increases (see theoretical explanation below): there is a factor of five decrease in $\delta_{\text{[CH] FWHM}}$ from 1 to 10 atm.

Simple physical arguments can be used to relate flame thickness to laminar flame speed. The flame region is usually divided in two successive regions: the preheat zone, within which reactant and heat diffusion take place, followed by the reaction zone, within which the chemical reactions are taking place. Activation energies are typically high in combustion processes, hence the reaction zone thickness, δ_{c}^0, is very thin compared to the preheat zone thickness, δ_{h}^0. In the preheat zone, convection balances diffusion:

$$t_{\text{convection}} \sim t_{\text{diffusion}} \ , \tag{8.2}$$

with $t_{\text{convection}} \sim \frac{\delta_{\text{h}}^0}{u}$ and $t_{\text{diffusion}} \sim \frac{(\delta_{\text{h}}^0)^2}{\left(\frac{\lambda}{\rho c_{\text{p}}}\right)}$ Therefore, using continuity: $\rho u = \rho_{-\infty} S_{\text{u}}^0$

$$\delta_{\text{h}}^0 \sim \frac{\left(\frac{\lambda}{c_{\text{p}}}\right)}{\rho_{-\infty} S_{\text{u}}^0} \ , \tag{8.3}$$

From an analysis of the flame region using high activation energy asymptotics, the laminar flame speed was shown to have a dependence on pressure of the following form:

$$S_{\text{u}}^0 \sim p^{\gamma} \ exp(-\frac{E_a}{2R^0 T_{\text{ad}}}) \ , \tag{8.4}$$

where

$$\gamma = \frac{n}{2} - 1 \tag{8.5}$$

where n is the overall reaction order, E_a is the overall activation energy (Arrhenius law) in cal/mole, R^0 is the universal gas constant equal to 1.987 cal/(mole.K), and T_{ad} is the adiabatic flame temperature. Both chemical reaction ($\frac{n}{2}$) and density variation (-1) appear in the dependence of S_{u}^0 on p. Eq. 8.4 then implies that $\delta_{\text{h}}^0 \sim \frac{\lambda}{c_p}/p^{\frac{n}{2}}$. Since $\left(\frac{\lambda}{c_p}\right)$ is not sensitive to pressure, δ_{h}^0 decreases as pressure increases.

A serious consequence is the experimental difficulty to resolve high pressure flames since they are so thin. It should be possible, however, to resolve flames up to moderate pressures, with the upgrade brought to our velocimetry technique discussed in the future work chapter, that will increase spatial resolution, thanks to a new high repetition-rate laser and by applying the correction for finite particle-track interval detailed in Bergthorson & Dimotakis (2005).

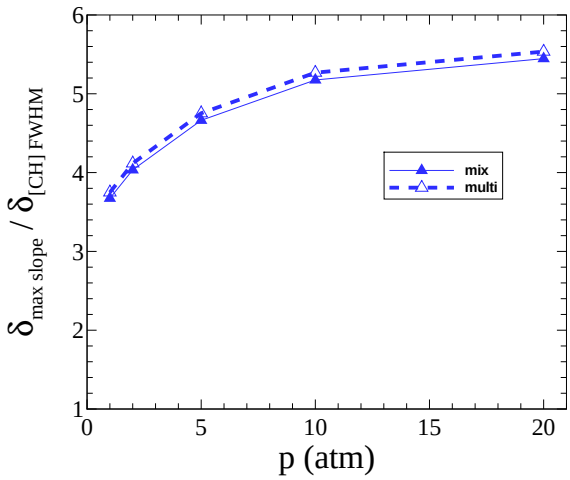

Figure 8.6: Comparison of flame thicknesses based on the [CH] FWHM and the tangent method, for a stoichiometric methane-air flame.

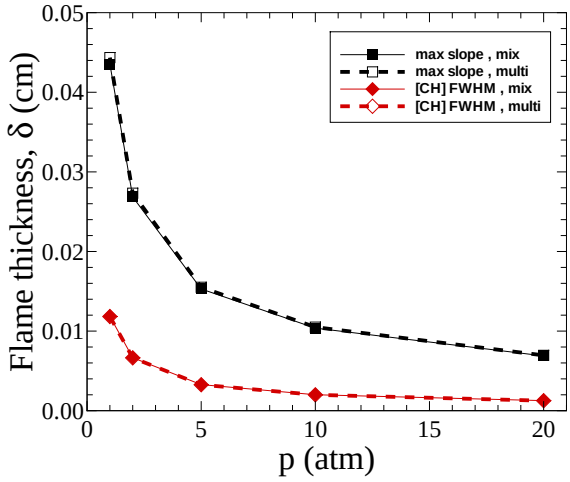

Figure 8.7: Variation of flame thickness with pressure, for a stoichiometric methane-air flame.

8.5 Comparative study of different mechanisms as pressure and equivalence ratios are changed

Figures 8.8-8.16 show the values of the laminar flame speeds predicted by the different mechanisms for p = 1,2,5,10,20 atm. Figures 8.18-8.22 show the values of the laminar flame speeds predicted by the different mechanisms for Φ = 0.6,1,1.4. For more clarity, for each mechanism the relative differences of their predictions and the predictions made by GRI-Mech 3.0 are plotted against equivalence ratio across the whole range of pressures on Fig. 8.9-8.17, and against pressure for the leanest, stoichiometric, and richest cases on Fig. 8.19-8.23.

The scatter between the different mechanisms tends to reach a minimum around stoichiometric conditions (still a 10% band, if we omit SD 200308, which consistently overpredicts flame speeds), and is maximum at the limit lean and rich cases (as much as 45% at 10 atm for lean regimes). This scatter tends to become larger as pressure increases. The main difference between the last version of the San-Diego mechanism SD 200506, compared to the previous one SD 200503, is that it predicts higher flame speeds in lean regimes. The C3-Davis generally predicts smaller values than the other mechanisms do; and at higher pressures (10 and 20 atm) as well as in lean regimes, this effect is significant. As pressure increases, the relative differences between mechanisms tends to stabilize closer to stoichiometric conditions, for rich regimes.

An important feature that is apparent from Fig.8.18-8.22 is that similar trends are obtained for the different mechanisms as pressure varies. If we compare to Fig. 8.9-8.17 which describe the composition effect, more differences seem to appear in the trends predicted by the different mechanisms. This would tend to imply that variable compositions are more challenging than variable pressures for the chemical kinetics mechanisms studied here.

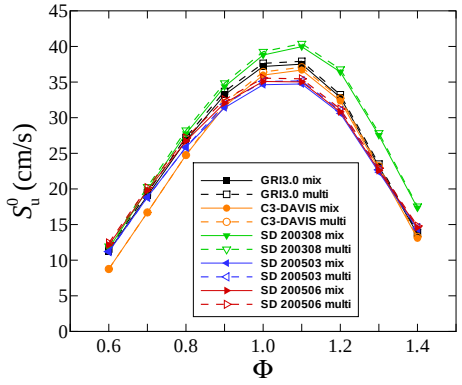

Figure 8.8: Laminar flame speeds predicted by the different mechanisms at p = 1 atm, for a methane-air flame.

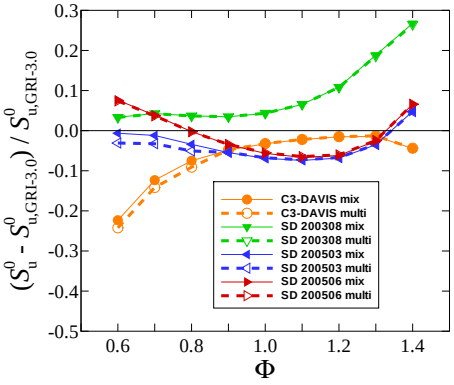

Figure 8.9: Comparison of the laminar flame speeds at p = 1 atm for different mechanisms, for a methane-air flame.

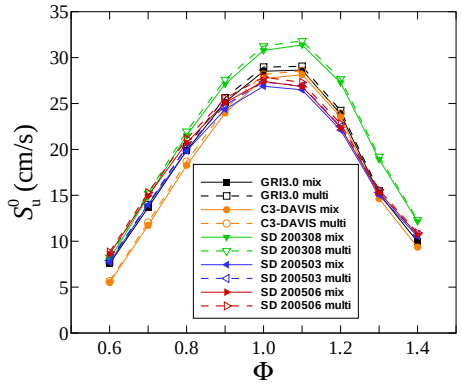

Figure 8.10: Laminar flame speeds predicted by the different mechanisms at p = 2 atm, for a methane-air flame.

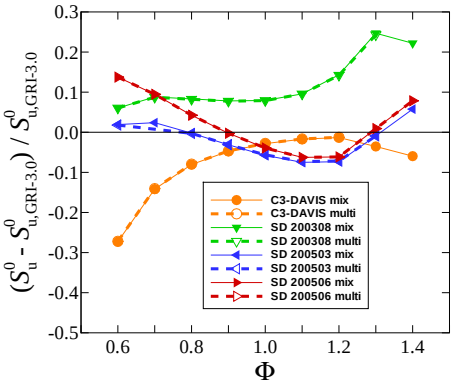

Figure 8.11: Comparison of the laminar flame speeds at p = 2 atm for different mechanisms, for a methane-air flame.

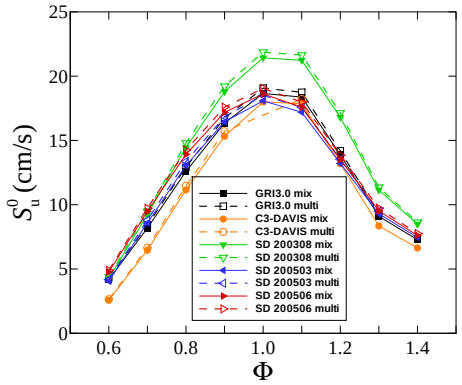

Figure 8.12: Laminar flame speeds predicted by the different mechanisms at p = 5 atm, for a methane-air flame.

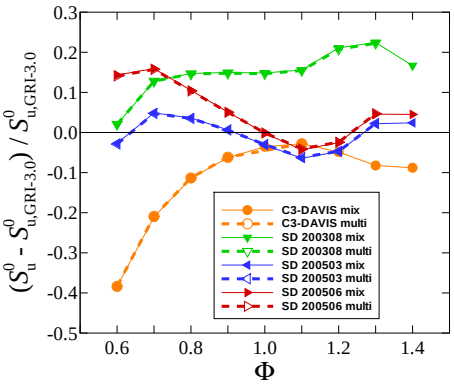

Figure 8.13: Comparison of the laminar flame speeds at p = 5 atm for different mechanisms, for a methane-air flame.

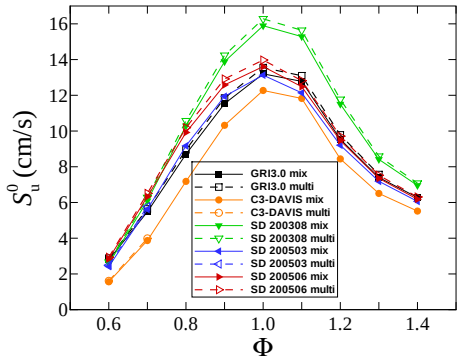

Figure 8.14: Laminar flame speeds predicted by the different mechanisms at p = 10 atm, for a methane-air flame.

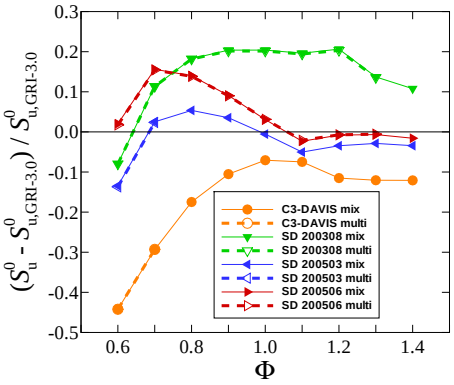

Figure 8.15: Comparison of the laminar flame speeds at p = 10 atm for different mechanisms, for a methane-air flame.

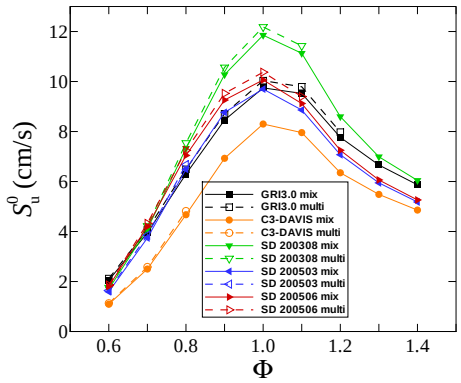

Figure 8.16: Laminar flame speeds predicted by the different mechanisms at p = 20 atm, for a methane-air flame.

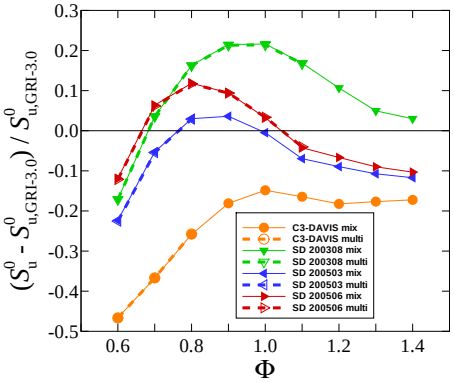

Figure 8.17: Comparison of the laminar flame speeds at p = 20 atm for different mechanisms, for a methane-air flame.

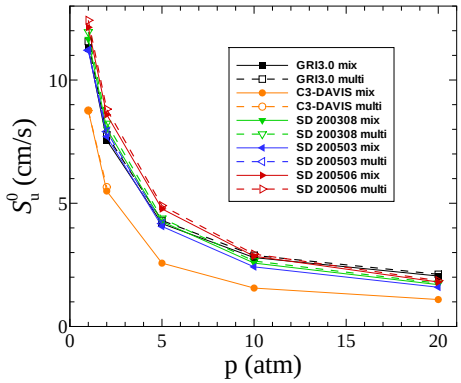

Figure 8.18: Comparison of the laminar flame speeds at Φ = 0.6 for different mechanisms, for a methane-air flame.

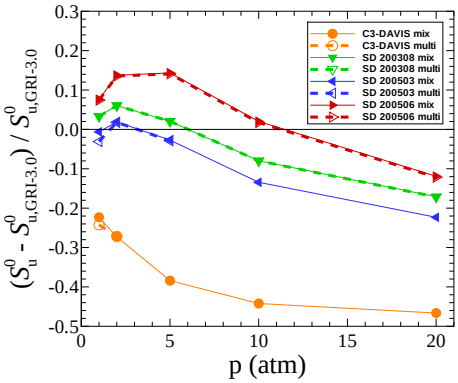

Figure 8.19: Comparison of the laminar flame speeds at Φ = 0.6 for different mechanisms, for a methane-air flame.

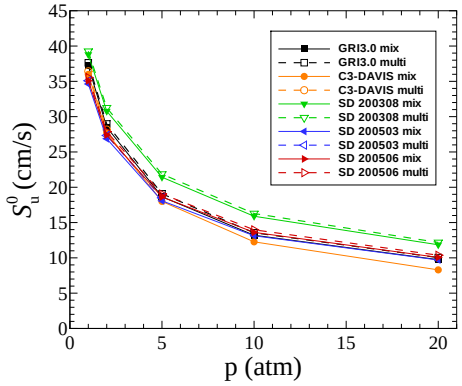

Figure 8.20: Comparison of the laminar flame speeds at $\Phi = 1$ for different mechanisms, for a methane-air flame.

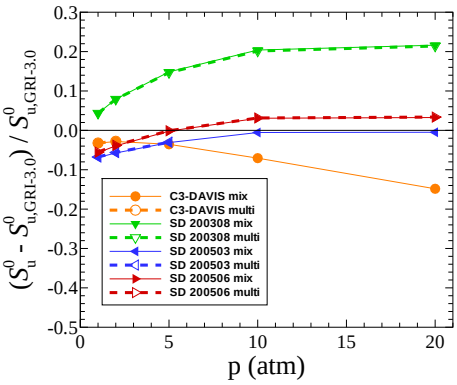

Figure 8.21: Comparison of the laminar flame speeds at $\Phi = 1$ for different mechanisms, for a methane-air flame.

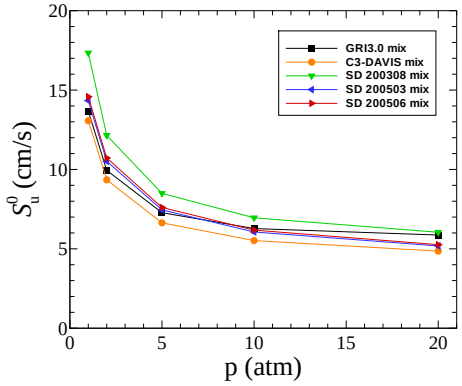

Figure 8.22: Comparison of the laminar flame speeds at $\Phi = 1.4$ for different mechanisms, for a methane-air flame.

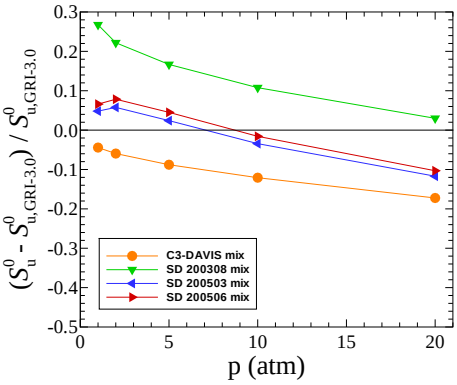

Figure 8.23: Comparison of the laminar flame speeds at $\Phi = 1.4$ for different mechanisms, for a methane-air flame.

Chapter 9

Conclusions

The technique developed by Bergthorson *et al.* (2005a) capable of testing chemistry, thermodynamic, and transport models through direct comparison with experiment was validated for methane-air flames. A repeatable discrepancy between predictions and experimental data occurs for the leanest flame: the flame speed is overestimated by GRI-Mech 3.0, and the two San-Diego mechanisms tested, whereas the C_3-Davis mechanism predicts it correctly. The richest $\Phi = 1.3$ flame experiment needs to be repeated.

As for the ethylene-air flames, although the cause of the sudden degradation of the different mechanisms performances from $\Phi = 1.6$ to $\Phi = 1.8$ was not identified, it turns out to be repeatable, and requires further investigation.

In order to fully constrain a combustion chemical-kinetics-transport model, experimental data must be provided over a wide range of parameters. The key parameters affecting flame propagation are fuel type, fuel composition, and pressure. The scatter between predictions of methane-air laminar flame speeds using different mechanisms increases with pressure, which indicates that progress must be made to better represent the competition between two-body and three-body reactions. While the design to bring the current experimental set-up at high pressures starts, some crucial work can be done with the two other parameters: fuel type and fuel composition. Thanks to the velocimetry upgrade, and a very flexible gas delivery system, the following fuels can be tested for different compositions: pure ethylene, blends of ethylene and hydrogen, propane, propylene, and diluted hydrogen. Independent streams of oxygen and diluent will enable measurements in very lean and very rich flames. They will also allow the decoupling of composition and heat release effects by modifying the ratio $O_2/(O_2 + \text{diluent})$, to conduct the variable composition study at a constant adiabatic flame temperaure. Furthermore, extinction studies at high wall temperatures will add extinction strain-rates to the experimental data pool, while being the first step towards capturing the dynamics of flame holes.

Chapter 10

Future work

10.1 Extinction

Although wall temperature has a weak effect on flame behavior, extinction by decreasing it is likely to happen for a lean CH_4-Air flame. Once extinction can be triggered repeatably via downstream heat loss, the mapping of extinction limits in terms of strain rate, equivalence ratio, and composition should be possible.

10.2 Laminar flame speeds

Comparisons will be made between laminar flame speeds determined by extrapolation to zero strain, using the CANTERA stagnation-flow code, and laminar flame speeds predicted by 1-D adiabatic, freely propagating flame simulations by CANTERA, CHEMKIN, and COSILAB.

10.3 Velocimetry diagnostic upgrade

To perform the PSV measurements, a continuous wave Argon-Ion laser operating at 2.5W is currently used. It is chopped at a 50% duty cycle and at a maximal frequency of 2.4kHz to illuminate the particles for a specified amount of time. The exposure on the CCD imager then consists of streaks that can be used to determine the local flow velocity. Using both the start-to-start and end-to-end streak information (Bergthorson *et al.* 2005a), the actual spatial resolution is determined from the flow velocity and from a repetition rate equal to twice the maximum chopping frequency, that is 4.8kHz. At the time the equipment was purchased, this way to track particles was state of the art. This method suits well the study of methane and ethane flames. However, as we are studying stronger fuels such as ethylene or hydrogen, and possibly blends of ethylene and hydrogen and nitric oxide (Egolfopoulos & Dimotakis 2000), the maximum velocities involved are significantly higher. Moreover, gradients are steeper at higher pressures (see Section 8.4). Such challenging

measurements require a higher spatial/temporal resolution than possible with the current technique. The whole velocity diagnostic (chiefly the light source) is therefore being upgraded to a higher level of performance in order to enable studies of stronger fuels and high pressure flames. A new high power, diode-pumped, green, Q-switched laser, with an average power greater than 75W at 5KHz will be used (the Evolution-75 model from Coherent). First the repetition rate achievable would range from 1KHz to 10KHz. Moreover thanks to a double-pulse capability, a sustained repetition-rate of 20kHz would be achievable, allowing us to measure velocities four times faster. The main difference between using a continuous wave laser which would be modulated and the diode-pumped Q-switched laser is that energy is not blocked half the time (50% duty cycle), but stored and released in short pulses (200ns at 5KHz), hence resulting in increased energy per pulse: 20mJ from 1kHz to 5kHz and more than 7.5mJ at 10kHz (instead of 1.25mJ at 1kHz and 0.52mJ at 2.4KHz with our current set-up). A higher resolution PCO-2000 Cooke camera will be used together with this laser (2k by 2k instead of 1k by 1k pixels) so that light-collecting will not limit the spatial resolution for the time separations between pulses that we are interested in. The technique that will be used is Particle Tracking Velocimetry (instead of Particle Streak Velocimetry used previously).

10.4 High pressures

In the chemical-kinetic mechanisms used to simulate combustion processes, as pressure varies, reaction rates of the three-body reactions (represented by the modified Arrhenius expression), and pressure-dependent reaction-rate expressions (fall-off reactions: Lindeman and Troe) change. The constants in these expressions are determined by optimization procedures based on experimental data such as ignition delays, species profiles, and laminar flame speeds. However due to the scarcity of experimental data combining flame propagation and species profiles at high pressures, upgrading the current experimental apparatus to allow moderately high pressures would be valuable.

10.5 Soot

An investigation will be conducted using the mechanism developed by Appel *et al.* (2000), special attention will be paid to acetylene (C_2H_2) and pyrene ($C_{16}H_{10}$), which are known precursors of soot, typically present in rich hydrocarbon flames, and more as pressure increases.

Appendix A

CANTERA simulations

Simulations of freely propagating flames and stagnation point flames were performed using the CANTERA software package developed by Goodwin (2003).

A.1 Convergence study for stagnation flame simulations

The convergence of the simulations was studied as a function of the number of grid points in the solution for both the stagnation-flow code and the adiabatic, freely propagating flame code, using mixture-averaged transport. The grid points are determined by an adaptive-mesh refinement technique that refines the solution based on three parameters: `ratio`, `curve`, and `slope`. The `ratio` parameter defines the maximum cell-length ratio between adjacent cells. The value `ratio` = 3.0 was chosen, so that the cell size is allowed to double between adjacent cells with a uniform initial grid. The `curve` parameter allows refinement in high-curvature regions. The value `curve` = 0.8 was found to give both good convergence and appropriate refinement in the high-curvature regions. The `slope` parameter allows refinement in high-gradient regions. The value of `slope` is reduced to add more grid points to the solution. An adaptive-mesh refinement technique of this type is especially needed in flame simulations.

Fig. A.1 shows the convergence of the maximum temperature, $T_{\max}$, maximum velocity, $u_{\max}$, and position of the maximum of the CH profile, x_{CH} in a stagnation flame. The percent error relative to the solution with the maximum number of grid points, N, is calculated for simulations at varying resolution, i, in the following way: $100 \times (T_{\max,i} - T_{\max,\mathrm{N}})/T_{\max,\mathrm{N}}$, $100 \times (u_{\max,i} - u_{\max,\mathrm{N}})/u_{\max,\mathrm{N}}$, $100 \times (x_{\mathrm{CH},i} - x_{\mathrm{CH,N}})/x_{\mathrm{CH,N}}$.

The values are seen to asymptote with a difference of less than 1 % when the number of grid points exceeds 300. As the number of grid points gets larger than 300, refinement occurs solely to resolve the N_2 species, although N_2 is inert and its profile should therefore stay flat. Time-integration tends to fail during that excessive refinement. This indicates that the refinement procedure is not working properly. Alternative refinement procedures will be implemented that use the following ideas:

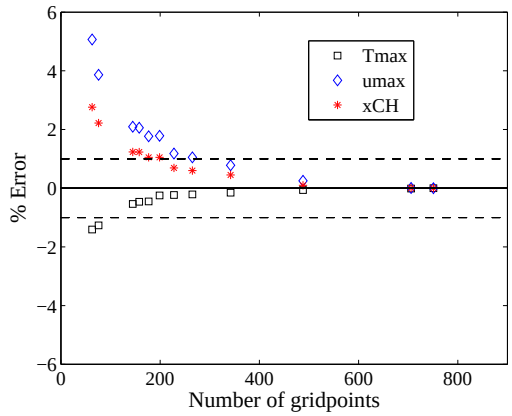

Figure A.1: Convergence study in a stagnation $\Phi = 1.0$ methane-air flame.

- enforcing refinement to ignore flat non zero species profiles,
- refinement focusing on both temperature and OH profile gradients,
- assessing characteristic chemical-reaction times at each grid-point and deducing the resolution required to resolve the flow around that point.

Appendix B

New plate design

The copper plate is the crucial piece, its design is shown in Fig. B.1. Copper was chosen for its high thermal conductivity. The plate-mass was reduced a maximum so that the thermal inertia is minimized (each experiment would require *a priori* that the plate be heated up to 1000K). The melting temperature of copper is 1358K, which is far enough from 1000K not to alter the copper properties. Seven K-thermocouples are used to monitor the temperature at 3 different axial and 5 different radial locations. To reduce the radiative heat loss which is significant at the high temperatures targeted, ceramics fibers are wrapped around the plate. The extra mass of copper at the bottom of the plate at the edges prevents the streamlines from being disturbed.

The other following pieces are chosen to be in stainless steel, because it exhibits a very low thermal conductivity, and thus contributes to insulate the copper plate. It also has a melting temperature of 1700K, which provides us a substantial margin above 1000K.

The mount ring shown in Fig. B.2 is bolted to the copper plate and linked to the mounts. It allows the plate to be lifted and its vertical position to be adjusted.

The plate cover described in Fig. B.3 then sits on the rims press-fitted on the mount ring, hence providing a seal effect which reduces the heat loss from the copper plate via radiations. At the same time the slots allow the hot gases to get out, which prevents some pressure building.

Helium flows through a 1/4" diameter tube, which is welded on the bottom surface of the ring described in Fig. B.4 in order to cool the copper plate. This ring leads the coolant gas towards the plate and makes it flow along it so that radial temperature gradients inside the plate will not be too high. As a consequence, the temperature gradient from the bottom part of the plate to the upper part of the plate is maximal at the center of the plate, which is suitable to trigger extinction at the center of the flame. The ring also insulates the helium cold gas from the helium warmed gas escaping from the plate. A 7/8" diameter tube is welded on the top surface of the ring to prevent the hot gases rising due to buoyancy to preheat the helium meant to cool the plate. This outer tube is able to slide through the center hole of the cover plate and is fixed by the split-collar shown in Fig. B.5, which is bolted onto the cover plate.

One advantage given by this design is that the whole cooling system (tubes welded to ring, fixed to cover plate) is easily removable at once since the cover plate only sits on the rims press-fitted on the mount ring.

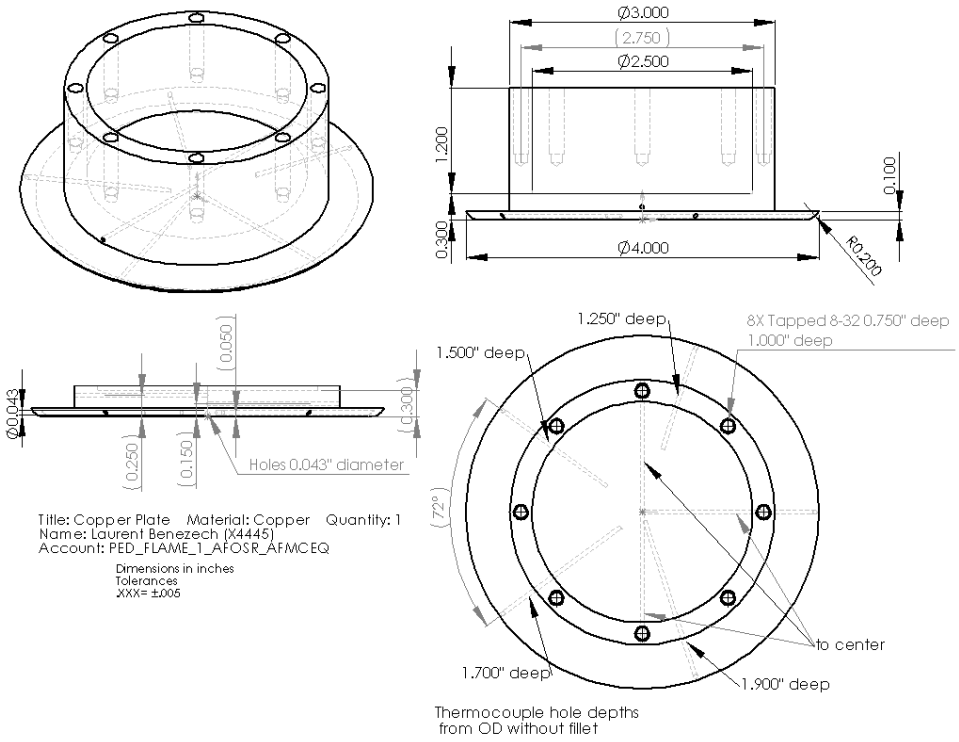

Figure B.1: Copper plate design

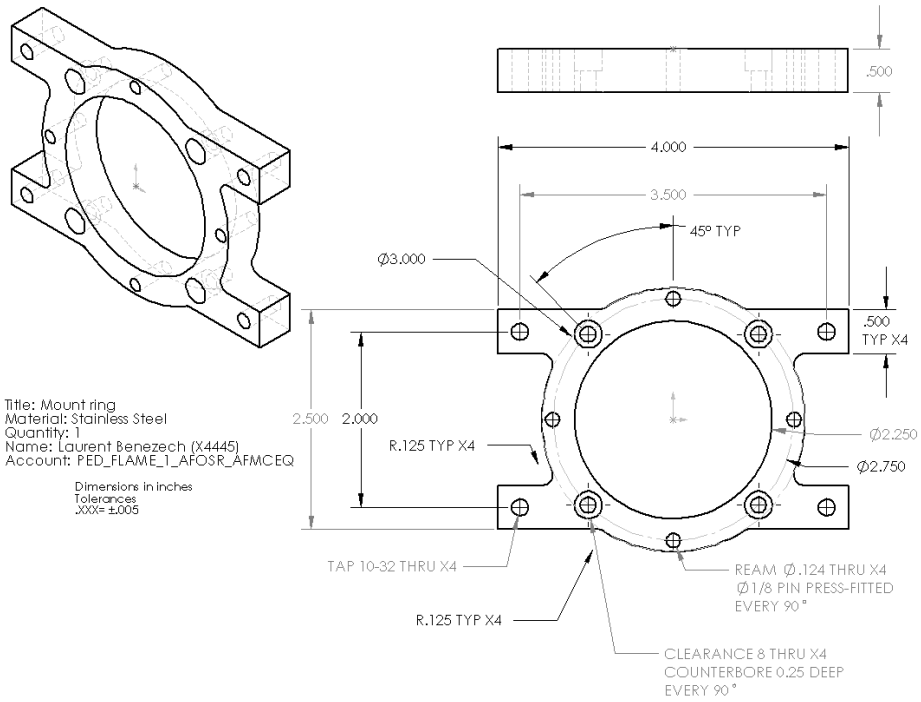

Figure B.2: Mount ring design

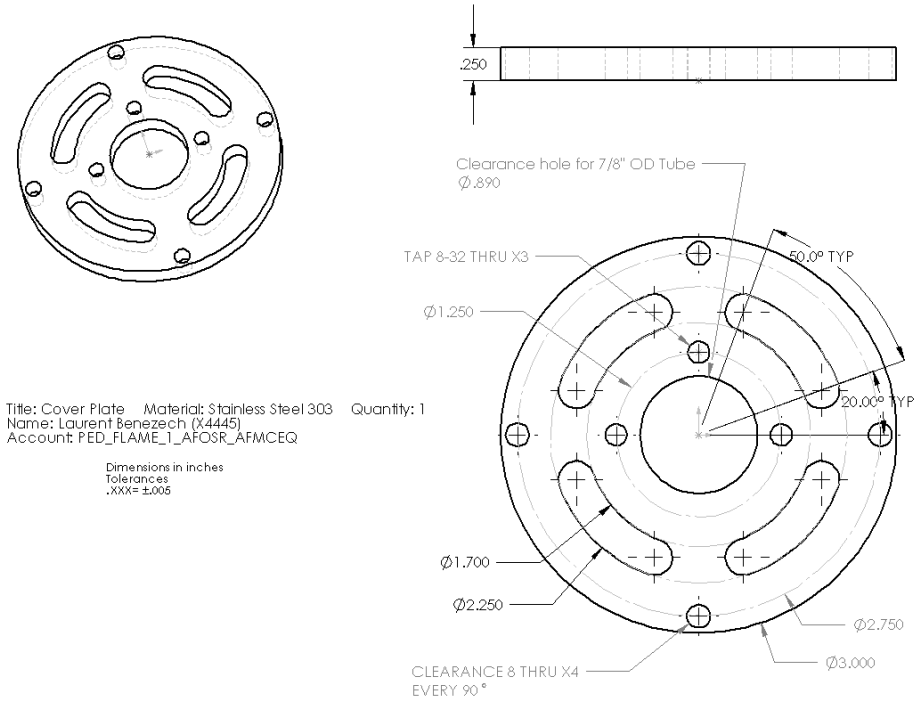

Figure B.3: Plate cover design

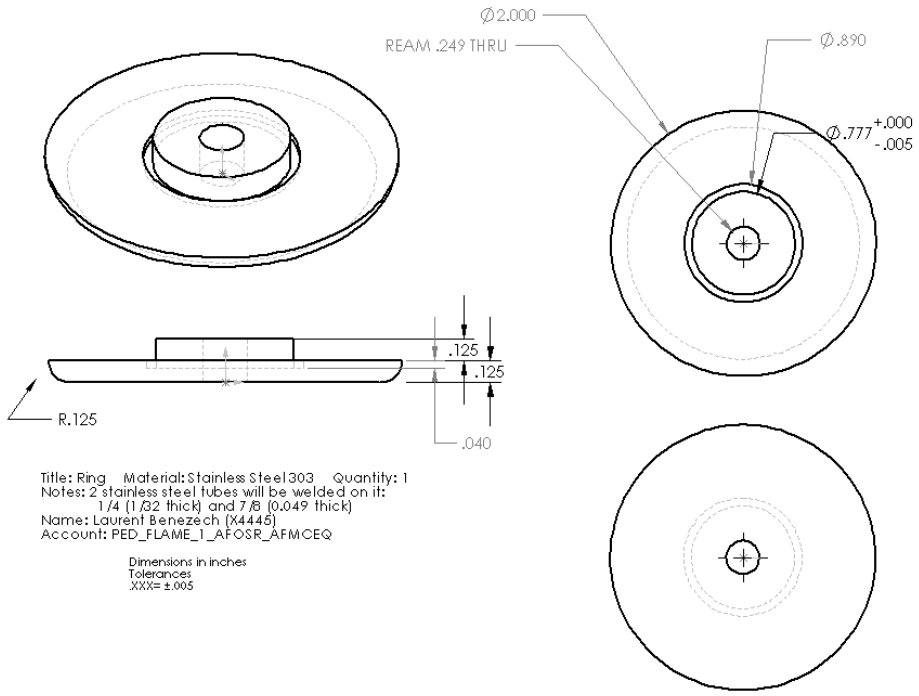

Figure B.4: Ring design

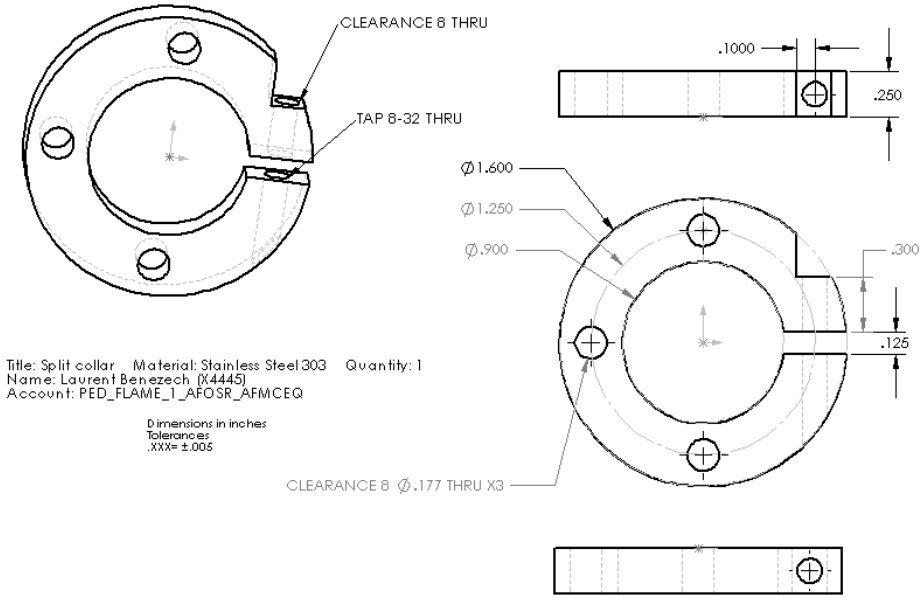

Figure B.5: Split collar design

Appendix C

Mass flow meter calibration

As shown in the flame chemistry effects chapter, the stagnation flames studied are very sensitive to equivalence ratio. The Omega FMA868-V 20 standard-Liter-per-minute (sLpm) thermal mass flow meter was used for the air stream, and the Omega FMA872-V 2 sLpm thermal mass flow meter was used for the methane stream. By recalibrating these flow meters, errors as high as 6% full-scale were discovered by Bergthorson (2005) although the specified accuracy is ±1% full-scale. However each thermal flow meter error due to nonlinearity in the voltage-flow response can be removed by calibrating it against a piston prover device (Bios International DryCal ML-500) of sufficient accuracy, over the entire range of the thermal flow meter, so that only random errors remain (Cf. repeatability) (Bergthorson 2005). Fig. C.1 plots the flow rate of methane measured by the DryCal ML-500, against a line representing the manufacturer-specified flow equation and a third-order fit performed to the data. The fit constants were found by fitting flow rates measured by the DryCal ML-500, to the corresponding voltage output of the thermal flow meter. A systematic error of up to 6% appears clearly in the manufacturer-specified flow-voltage relationship in Fig. C.2, which plots the error between the flow-rate measured by the DryCal ML-500 and the thermal mass flow meter, using the manufacturer-specified flow-voltage relationship, and the new cubic representation.

The % full-scale error is calculated as

$$\%\,\mathrm{FS\ error} = 100 \times \frac{Q_\mathrm{t} - Q_{\mathrm{ML}-500}}{Q_{\mathrm{t,FS}}}\ , \tag{C.1}$$

where Q_t is the volume flowrate measured by the thermal mass flow meter, $Q_{\mathrm{t,FS}}$ is the maximum, or full-scale, flowrate for the thermal mass flow meter, and $Q_{\mathrm{ML}-500}$ is the volume flowrate measured by the DryCal ML-500 piston-prover. Q_t is calculated from the measured voltage output of the flow meter using the appropriate calibration function (linear or cubic).

Fig. C.3 and C.4 plot both the full-scale and relative error between the DryCal ML-500 measurements and the calibrated thermal flow meters for methane, and air.

Note that only a selected number of calibration datasets have been included in these plots for

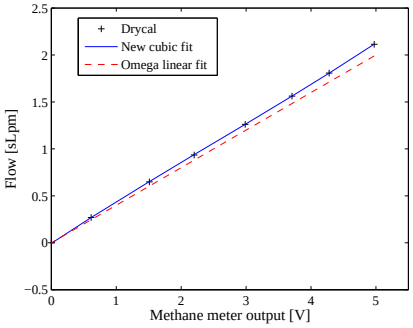

Figure C.1: Comparison of methane flow rate measured using DryCal ML-500 to the manufacturer specified flow-voltage relation and the new cubic fit to the data.

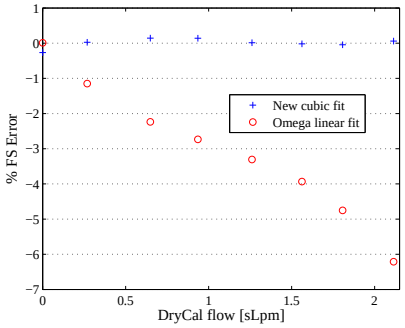

Figure C.2: Full-scale error compared to DryCal ML-500 flow rate for the manufacturer specified calibration and the new cubic fit.

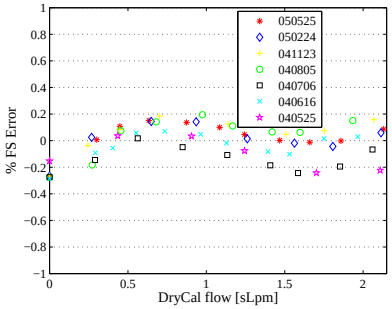

(a) Full-scale error

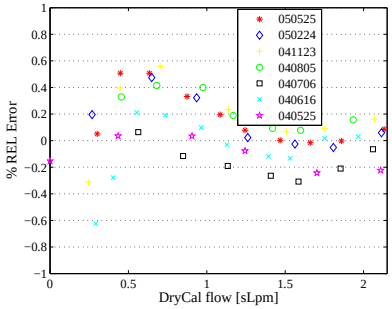

(b) Relative error

Figure C.3: Full-scale and relative error for methane flow meter compared to DryCal ML-500 measurements. Calibrations from several dates are included to indicate the stability of the devices over extended periods of time.

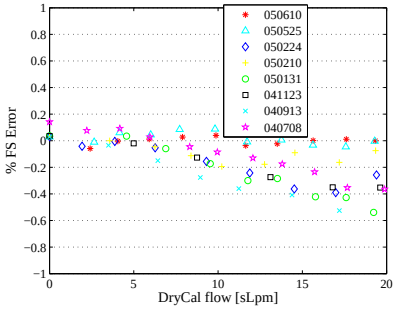

(a) Full-scale error

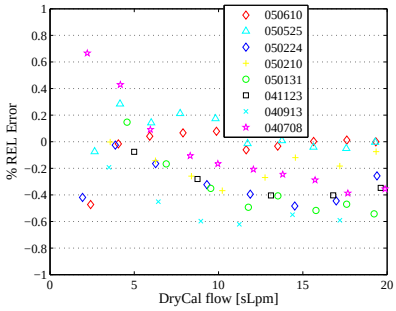

(b) Relative error

Figure C.4: Full-scale and relative error for air flow meter compared to DryCal ML-500 measurements.

clarity. The relative error is defined as

$$\%\,\mathrm{REL\ error} = 100 \times \frac{Q_\mathrm{t} - Q_\mathrm{ML-500}}{Q_\mathrm{ML-500}} \ , \tag{C.2}$$

where the value of the flowrate at the current setting is utilized to normalize the difference, rather than the full-scale flowrate.

The full-scale error tends to be less than $\pm\,0.2\%$ for the methane flow meter, in accord with the manufacturer specified repeatability of the instrument. As for the air flow meter, it has recently undergone a drift, which has been taken into account by refitting to newer data, so that the full-scale error also tends to be less than $\pm\,0.2\%$.

C.1 Uncertainty in equivalence ratio

Although a cubic fit is used to represent the relation between output voltage from the flow meter V and flow-rate Q_t: $Q_\mathrm{t} = \alpha + \beta\ V + \gamma\ V^2 + \delta\ V^3$, only the linear contribution will show up in the uncertainty analysis, since α is fixed, $\gamma, \delta << \beta$ typically, and chiefly since the uncertainty in V is small, the uncertainty in V^2 and V^3 is even smaller. Thus

$$(\frac{\sigma_\mathrm{Q_t}}{< Q_\mathrm{t} >})^2 = (\frac{\sigma_\beta}{< \beta >})^2 + (\frac{\sigma_\mathrm{V}}{< V >})^2 \ , \tag{C.3}$$

where σ is the root mean square, and $< . >$ is the average.
As the flow meters are typically used in the top-half of their flow range, the relative error is typically $\pm\,0.2$–0.4%, hence $\frac{\sigma_\mathrm{V}}{<V>} = 0.4\%$. Moreover, the DryCal has an associated uncertainty of $\pm\,0.4\%$ in the mass-flow measurements, hence $\frac{\sigma_\beta}{<\beta>} = 0.4\%$. Therefore $\frac{\sigma_\mathrm{Q_t}}{<Q_\mathrm{t}>} = 0.6\%$.

The equivalence ratio is defined by

$$\Phi \equiv \frac{\frac{Q_\mathrm{t,F}}{Q_\mathrm{t,O}}}{(\frac{Q_\mathrm{t,F}}{Q_\mathrm{t,O}})_{\Phi=1}} \ , \tag{C.4}$$

where $Q_\mathrm{t,F}$ and $Q_\mathrm{t,O}$ are respectively the flow-rates of fuel (methane here) and oxidizer (air here), and where the stoichiometric fuel to oxidizer ratio, $(\frac{Q_\mathrm{t,F}}{Q_\mathrm{t,O}})_{\Phi=1}$, is determined as the ratio of moles of fuel to moles of oxidizer required for complete conversion of the reactants into products. This ratio is $(\frac{Q_\mathrm{t,F}}{Q_\mathrm{t,O}})_{\Phi=1} = \frac{1}{9.52}$ for a methane-air mixture. The measures of $Q_\mathrm{t,F}$ and $Q_\mathrm{t,O}$ are uncorrelated, and we assume $\frac{\sigma_\mathrm{Q_{t,F}}}{<Q_\mathrm{t,F}>} = \frac{\sigma_\mathrm{Q_{t,O}}}{<Q_\mathrm{t,O}>}$, therefore

$$(\frac{\sigma_\Phi}{< \Phi >})^2 = 2(\frac{\sigma_\mathrm{Q_t}}{< Q_\mathrm{t} >})^2 \ , \tag{C.5}$$

This yields an estimated uncertainty in the equivalence ratio, $\frac{\sigma_\Phi}{<\Phi>} = 0.8\%$.

Bibliography

Ancimer, R., Wallace, J., & Jääskeläinen, H., 1999. Investigations into the effect of LDV seed particles on the operating characteristics of a spark ignition engine. *Experiments in Fluids*, **27**:175–180.

Appel, J., Bockhorn, H., & Frenklach, M., 2000. Kinetic modeling of soot formation with detailed chemistry and physics: laminar premixed flames of c_2 hydrocarbons. *Combustion & Flame*, **121**:122–136.

Bergthorson, J. M., 2005. *Experiments and modeling of impinging jets and premixed hydrocarbon stagnation flames*. Ph.D. thesis, California Institute of Technology.

Bergthorson, J. M. & Dimotakis, P. E., 2005. Particle velocimetry in high-gradient/-curvature flows. *Experiments in Fluids*. (accepted).

Bergthorson, J. M. & Dimotakis, P. E., 2006. Premixed laminar $C_1 - C_2$ stagnation flames: experiments and simulations with detailed thermochemistry models. *Proceedings of the Combustion Institute*. (submitted).

Bergthorson, J. M., Goodwin, D. G., & Dimotakis, P. E., 2005a. Particle streak velocimetry and CH laser-induced fluorescence diagnostics in strained, premixed, methane-air flames. *Proceedings of the Combustion Institute*, **30**:1637–1644.

Bergthorson, J. M., Sone, K., Mattner, T. W., Dimotakis, P. E., Goodwin, D. G., & Meiron, D., 2005b. Impinging laminar jets at moderate reynolds numbers and separation distances. *Physical Review E*, **72**.

Crosley, D. R., 1989. Semiquantitative laser-induced fluorescence in flames. *Combustion & Flame*, **78**:153–167.

Davis, S. G., Law, C. K., & Wang, H., 1999. Propene pyrolysis and oxidation kinetics in a flow reactor and laminar flames. *Combustion & Flame*, **119**:375–399.

Dixon-Lewis, G., 1968. A fortran computer code package for the evaluation of gas-phase multicomponent transport properties. *Proceedings of the Royal Society of London Series A–Mathematical and Physical Sciences*, **A304**:111–135.

Egolfopoulos, F. N. & Dimotakis, P. E., 2000. Effects of additives on the non-premixed ignition of ethylene in air. *Combustion Science & Technology*, **156**:173–199.

Egolfopoulos, F. N., Zhang, H., & Zhang, Z., 1997. Wall effects on the propagation and extinction of steady, strained, laminar premixed flames. *Combustion & Flame*, **109**:237–252.

Goodwin, D. G., 2003. An open-source, extensible software suite for CVD process simulation. In *Proc. of CVD XVI and EuroCVD Fourteen,* Electrochem. Soc., pages 155–162.

Gu, X. J., Haq, M. Z., Lawes, M., & Woolley, R., 2000. Laminar burning velocity and markstein lengths of methane-air mixtures. *Combustion & Flame*, **121**:41–58.

Kee, R. J., Coltrin, M. E., & Glarborg, P., 2003. *Chemically Reacting Flow - Theory & Practice*. John Wiley & Sons, Inc., New Jersey.

Metghalchi, M. & Keck, J. C., 1980. Laminar burning velocity of propane-air mixtures at high-temperature and pressure. *Combustion & Flame*, **38(2)**:143–154.

Nayagam, V. & Williams, F. A., 2002. Lewis-number effects on edge-flame propagation. *Journal of Fluid Mechanics*, **458**:219–228.

Nishioka, M., Law, C. K., & Takeno, T., 1996. A flame-controlling continuation method for generating S-curve responses with detailed chemistry. *Combustion & Flame*, **104**:328–342.

San Diego mechanism. Chemical-kinetic mechanisms for combustion applications, Center for Energy Research (Combustion Division), University of California at San Diego. `http://maeweb.ucsd.edu/combustion/cermech/`.

Smith, G. P., Golden, D. M., Frenklach, M., Moriarty, N. W., Eiteneer, B., Goldenberg, M., Bowman, C. T., Hanson, R. K., Song, S., Gardiner, W. C., Jr., Lissianski, V. V., & Qin, Z. GRI-Mech 3.0. `http://www.me.berkeley.edu/gri_mech/`.

Sutton, J. A. & Driscoll, J. F., 2003. Optimization of CH fluorescence diagnostics in flames: range of applicability and improvements with hydrogen addition. *Applied Optics*, **42**:2819–2828.

Yahagi, Y., Ueda, T., & Mizomoto, M., 1992. Extinction of lean methane/air turbulent premixed flames in a stagnation point flow. *Proceedings of the Combustion Institute*, **24**:537–542.